

Molecule formation in dust-poor irradiated jets

I. Stationary disk winds

B. Tabone^{1,2} *, B. Godard^{2,3}, G. Pineau des Forêts^{2,4}, S. Cabrit², E. F. van Dishoeck^{1,5}

¹ Leiden Observatory, Leiden University, PO Box 9513, 2300 RA Leiden, The Netherlands

² LERMA, Observatoire de Paris, PSL Research Univ., CNRS, Sorbonne Univ., 75014 Paris, France

³ Laboratoire de Physique de l'École normale supérieure, ENS, Université PSL, CNRS, Sorbonne Université, Université Paris-Diderot, Sorbonne Paris Cité, 75005 Paris, France

⁴ Université Paris-Saclay, CNRS, Institut d'Astrophysique Spatiale, 91405, Orsay, France

⁵ Max-Planck-Institut für Extraterrestrische Physik, Giessenbachstrasse 1, 85748 Garching, Germany

March 5, 2020

ABSTRACT

Context. Recent ALMA observations suggest that the highest velocity part of molecular protostellar jets ($\gtrsim 80 \text{ km s}^{-1}$) are launched from the dust-sublimation regions of the accretion disks ($\lesssim 0.3 \text{ au}$). However, formation and survival of molecules in inner protostellar disk winds, in the presence of a harsh far-ultraviolet (FUV) radiation field and the absence of dust, remain unexplored.

Aims. We aim at determining if simple molecules such as H_2 , CO , SiO , and H_2O can be synthesized and spared in fast and collimated dust-free disk winds or if a fraction of dust is necessary to explain the observed molecular abundances.

Methods. This work is based on a recent version of the Paris-Durham shock code designed to model irradiated environments. Fundamental properties of the dust-free chemistry are investigated from single point models. A laminar 1D disk wind model is then built using a parametric flow geometry. This model includes time-dependent chemistry and the attenuation of the radiation field by gas-phase photoprocesses. The influence of the mass-loss rate of the wind and of the fraction of dust on the synthesis of the molecules and on the attenuation of the radiation field is studied in detail.

Results. We show that a small fraction of H_2 ($\leq 10^{-2}$), primarily formed through the H^- route, can efficiently initiate molecule synthesis such as CO and SiO above $T_{\text{K}} \sim 800 \text{ K}$. We also propose new gas-phase formation routes of H_2 that can operate in strong visible radiation fields, involving for instance CH^+ . The attenuation of the radiation field by atomic species (eg. C, Si, S) proceeds through continuum self-shielding. This process ensures efficient formation of CO , OH , SiO , H_2O through neutral-neutral reactions, and the survival of these molecules. Class 0 dust-free winds with high mass-loss rates ($\dot{M}_{\text{w}} \geq 2 \times 10^{-6} M_{\odot} \text{ yr}^{-1}$) are predicted to be rich in molecules if warm ($T_{\text{K}} \geq 800 \text{ K}$). Interestingly, we also predict a steep decrease in the SiO -to- CO abundance ratio with the decline of mass-loss rate, from Class 0 to Class I protostars. The molecular content of disk winds is very sensitive to the presence of dust and a mass-fraction of surviving dust as small as 10^{-5} significantly increases the H_2O and SiO abundances.

Conclusions. Chemistry of high velocity jets is a powerful tool to probe their content in dust and uncover their launching point. Models of internal shocks are required to fully exploit the current (sub-)millimeter observations and prepare future JWST observations.

Key words. Stars: formation – ISM: jets & outflows – ISM: astrochemistry

1. Introduction

Protoplanetary disks provide their host accreting star with material and regulate the formation, growth, and migration of planets. The global evolution and dispersal of disks around nascent stars is regulated by the transport of angular momentum and mass-loss processes (Armitage 2011). Fast jets¹ are ubiquitously observed in accreting young stars of all ages, with universal collimation and connection between accretion and ejection, probably of magnetic origin (Cabrit 2002, 2007b). However, the region of the disk actually involved in mass ejection, and the associated angular momentum extraction, remain a topic of hot debate.

The main observational method proposed so far to locate the launching region of jets relies on the joint measurement of rotation and axial velocities (Anderson et al. 2003; Ferreira et al.

2006). While studies of atomic jets are currently limited by spectral resolution in the optical range (De Colle et al. 2016), the unique combination of high spectral ($< 0.5 \text{ km s}^{-1}$) and spatial (50 mas) resolution of ALMA now allows to conduct similar tests on jets from the youngest protostars, so-called Class 0, which are much brighter in molecules (eg. Tafalla et al. 2010) than jets from more evolved protostars and pre-main sequence stars (Class I and II) which are mainly atomic. In this context, high angular resolution observations ($\approx 8 \text{ au}$) of the fastest part of the HH 212 jet have unveiled rotation signatures in SiO emission suggestive of a disk wind launched within 0.3 au (Lee et al. 2017; Tabone et al. 2017). Owing to the high bolometric luminosity of the central protostar ($L_{\text{bol}} \approx 9L_{\odot}$, Zinnecker et al. 1992), dust is expected to be sublimated within 0.3 au, and the HH212 SiO -rich jet would thus trace a dust-free magnetohydrodynamic (MHD) disk wind.

To test the likelihood of this interpretation, it is now of paramount importance to check if the presence of SiO molecules in the jet of HH 212 is indeed compatible with a dust-free disk

* tabone@strw.leidenuniv.fr

¹ In this paper, "jet" refers to observed fast ($\gtrsim 50 \text{ km s}^{-1}$) and collimated (opening angle $\leq 8^\circ$) outflowing gas whereas "wind" refers to theoretical models that account for the origin of jets.

wind origin, as suggested by the rotation kinematics. Detailed astrochemical modeling of dusty magnetized disk winds show that molecules can survive the acceleration and the far-ultraviolet (FUV) field emitted by the accreting protostars (Panoglou et al. 2012). However, molecule formation in dust-free disk winds remains an open question. In the absence of dust, the FUV field can more easily penetrate the unscreened flow and photodissociate molecules, whereas H_2 formation on grains, the starting point of molecule synthesis, is severely reduced. So far, astrochemical models have only investigated dust-free winds launched from the stellar surface. Pioneering studies have shown that they are hostile to the formation of H_2 , due to photodetachment of the key intermediate H^- by visible photons from the star (Rawlings et al. 1988; Glassgold et al. 1989; Ruden et al. 1990), whereas other molecules such as CO, SiO or H_2O are destroyed when a strong UV excess is included (Glassgold et al. 1991). However, there have been yet no similar investigations in a disk wind geometry, and with a fully self-consistent FUV field.

The origin of the observed molecules in Class 0 jets is actually still debated, as high-velocity molecular emission is not necessarily tracing a pristine wind. Instead of assuming that molecules are material ejected from the vicinity of the star ("wind" scenario), another class of scenarios proposes that molecules are "entrained" by a fast and unseen atomic jet through bow-shocks or turbulence (Raga & Cabrit 1993; Canto & Raga 1991). Even if observations of small-scale molecular micro-jets ($\approx 10 - 400$ au, Cabrit et al. 2007; Lee et al. 2017) may contradict entrainment of envelope material, a slow dusty disk wind surrounding the fast jet could still bring fresh molecular material close to the jet axis and explain the observed collimation properties of molecular jets (White et al. 2016; Tabone et al. 2018). Observational diagnostics of the wind launch radius based on rotation signatures would not be reliable anymore in such time-variable jets (eg. Fendt 2011) or in jets prone to turbulent mixing.

In contrast with an inner disk wind scenario, the entrainment scenario implies that molecular material is rich in dust. Chemistry can then be used as a powerful diagnostic. Early astrochemical models of stellar winds already pointed-out unique features of dust-free chemistry such as a low CO/ H_2 ratio (Glassgold et al. 1989). It suggests that chemistry is a promising diagnostic of the dust content, and as such, could distinguish between dust-free disk wind and entrainment scenario. However, because sublimation temperature depends on the composition and sizes of grains, jets launched from the dust sublimation region of silicate and carbonaceous grains may contain a small fraction of surviving dust such as aluminum oxide grains (Al_2O_3) for which sublimation temperature is higher, ≈ 1700 K (Lenzuni et al. 1995). Despite representing a small mass-fraction of the total interstellar dust ($\approx 2\%$, assuming solar elemental abundances, Asplund et al. 2009), aluminum oxide grains could have a strong impact on the chemistry and bias the proposed test. Understanding the precise impact of a non-vanishing fraction of dust on the chemistry is thus an important step to distinguish "wind" to "entrainment" scenario.

Determining if molecular jets are indeed launched within the dust sublimation radius is a crucial question, as they would then bring new clues to planet formation theories. Recent studies suggest that the first steps of planet formation may occur in the protostellar phase (eg. Greaves & Rice 2010; Manara et al. 2018; Harsono et al. 2018). Probing the bulk elemental composition and inner depletion pattern of the inner gaseous regions of protoplanetary disks within the dust sublimation radius is a powerful tool to uncover key disk processes related to planet forma-

tion such as dust trapping in the outer parts of the disks (McClure & Dominik 2019; McClure 2019). However, deeply embedded Class 0 disks are too extinguished to be probed by optical and near-infrared atomic lines. Hence, if protostellar molecular jets are tracing a pristine dust-free disk wind, they would offer a unique opportunity to have access to the elemental composition of the inner region of Class 0 disks, and thus reveal elusive disk processes. In this perspective, observations of high-velocity molecular bullets toward active protostars show abundant oxygen-bearing species (SiO, SO) but a drop in carbon-bearing species such as HCN or CS that was interpreted as a low C/O ratio (Tafalla et al. 2010; Tychoniec et al. 2019). However, it remains unclear if abundance ratios of molecular tracers are indeed directly related to a change in elemental abundances rather due to unique features of dust-poor chemistry or shocked gas. A fine understanding of the chemistry operating in dust-free or dust-poor jets is required to use molecular jets as a probe of elemental abundances of the inner disks.

In the present paper, we revisit pioneering astrochemical models of stellar winds by investigating if molecules can be formed in a disk wind launched within the dust sublimation radius. We focus our analysis on H_2 and on the most abundant oxygen-bearing molecules observed toward protostellar jets, namely CO, SiO, OH, and H_2O (eg. Tafalla et al. 2010; Kristensen et al. 2011). Sulfur and nitrogen chemistry, as well as the dependency of molecular abundances on elemental ratios is beyond the scope of the present paper. Throughout this work, special attention is paid to the impact of a small fraction of dust on the chemistry to determine if molecular abundances can be used as a discriminant diagnostic even when the wind contains surviving refractory dust. The thermal balance, together with shock models will be presented in the next paper of this series.

In Section 2, we present the basic physical and chemical ingredients of the astrochemical model. For sake of generality, we then study molecule formation with the use of single point models (Section 3). It allows us to derive simple criteria for molecules to be abundant, as well as to specify their formation routes. More realistic models assuming a specific flow geometry are explored in Section 4. In contrast with single-point models, they include the effect of the dilution of the radiation field and density, time-dependent chemistry, and shielding of the radiation field. Limitations of the model, as well as observational diagnostics of dust-free and dust-poor winds are discussed in Section 5. Our findings are summarized Section 6.

2. Numerical method

Models presented throughout this work are based on the publicly available Paris-Durham shock code initially designed to compute the dynamical, thermal and chemical evolution of a plane-parallel steady-state shock wave. The code includes detailed microphysical processes and a comprehensive time-dependent chemistry (Flower & Pineau des Forêts 2003; Lesaffre et al. 2013). The versatility of this code allows computing also the thermal and chemical evolution of any 1D stationary flow in a slab approach. In this work, the recent version developed by Godard et al. (2019), which includes key processes of photon-dominated region (PDR) physics, has been further upgraded to ensure proper treatment of dust-free chemistry². Two types of model have been computed: single spatial point models (Section 3), and specific wind models (Section 4). We present here the

² the updated version of the code and former versions are available on the ISM platform <http://ism.obspm.fr>.

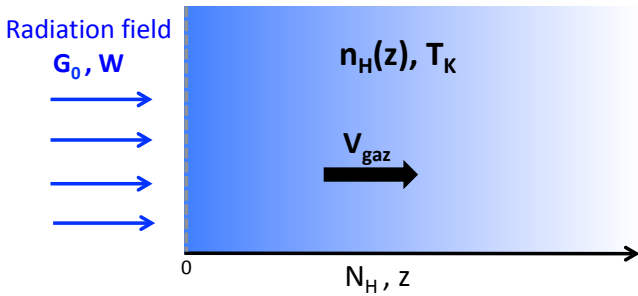


Fig. 1. Schematic view of the 1D geometry used in this work. The code solves the chemical evolution of a slab of gas flowing at a constant velocity V_{gas} and irradiated from the left (upstream) along a direction parallel to the flow. The proton density profile $n_{\text{H}}(z)$ is prescribed and the temperature T_{K} is constant. The radiation field is the sum of a FUV part modeled by an ISRF scaled by G_0 and a visible part modeled by a black body radiation field at $T_{\text{vis}} = 4000$ K diluted by a factor W (see Appendix A). The attenuation of the radiation field by gas-phase photoprocesses and by dust (if any) along z is computed consistently.

basic numerical method used in this work. Details on the specific wind model, including the prescribed density structure, are given in Section 4.1.

2.1. Geometry and parameters

Figure 1 gives a schematic view of the adopted geometry from which specific models can be built. The model is a slab of gas flowing at a velocity V_{gas} along the direction z and irradiated upstream ($z = 0$ in Fig.1). The proton density $n_{\text{H}}(z) = n(\text{H}) + 2n(\text{H}_2) + n(\text{H}^+)$ along the slab is also prescribed. Throughout this work, the gas is assumed to be isothermal with the kinetic temperature T_{K} . This allows us to study the influence of the temperature on the chemistry in a parametric way and independently of uncertainties in the thermal balance.

The impinging radiation field is parametrized as a sum of a FUV component modeled as a standard interstellar radiation field (ISRF, Mathis et al. 1983) scaled by a parameter G_0 plus a visible component modeled as a black-body radiation field at $T_{\text{vis}} = 4000$ K diluted by a factor³ W . The adopted functional form of the FUV field, as well as the shape of the resulting unshielded radiation field, are given in Appendix A.

2.2. Radiative transfer and photodestruction processes

The attenuation of the radiation field between $\lambda = 91$ nm and $1.5\mu\text{m}$ through the slab is computed by considering absorption by continuous photoprocesses along rays perpendicular to the slab and parallel to the flow. The attenuation coefficient due to gas-phase processes is then

$$\kappa_G(z, \lambda) = \sum_i \sigma_i(\lambda) n_i(z), \quad (1)$$

where $\sigma_i(\lambda)$ is the cross-section of the photoprocess involving the species X_i and n_i its particle number density. When dust is included, we assume that the grain size follows a power-law distribution of index -3.5 with a minimum and maximum size of

³ The shape of the visible part gives a reasonable approximation of the standard interstellar radiation field for $W \approx 5 \times 10^{-13}$ (see Appendix A), and a good proxy for the visible field close to nascent low-mass stars with $W = 5 \times 10^{-7} (R/10 \text{ au})^{-2}$, where R is the distance to the star and where we assume a stellar radius of $3R_{\odot}$.

$0.01 \mu\text{m}$ and $0.3 \mu\text{m}$, respectively (Mathis et al. 1977). Following Godard et al. (2019) (see their Appendix B) and for simplicity, absorption of UV photons by grains is calculated assuming the absorption coefficient of single size spherical graphite grains of radius $a_g = 0.02 \mu\text{m}$ derived by Draine & Lee (1984) and Laor & Draine (1993), where $a_g \equiv \sqrt{\langle r_c^2 \rangle}$ is calculated from the mean square radius of the grains.

Photodissociation and photoionization rates are computed following two different approaches. If the photoprocess leads to a significant attenuation of the FUV field or if it is a key destruction or formation pathway for a major species, then its rate is consistently computed by integrating the cross-section over the local radiation field including its UV and visible components (see Appendix A). Accordingly, the model includes absorption of photons by photoionization of C, S, Si, Mg, Fe, H^- , H_2O , SO, O_2 , and CH, and photodissociation of OH, H_2O , SiO, CN, HCN, H_2O , H_2^+ , SO, SO_2 , O_2 , CH^+ and CH. Cross-sections are taken from Heays et al. (2017) and subsequently resampled on a coarser grid of irregular sampling (about 100 points) to reduce computing time.

Alternatively, rates associated with other continuous photoprocesses are assumed to depend linearly on the integrated FUV radiation field as

$$k_{\text{photo}} = \alpha \frac{F(z)}{F_{\text{ISRF}}}, \quad (2)$$

where F_{ISRF} is the FUV photon flux from 911 \AA to 2400 \AA associated with the isotropic standard interstellar radiation field (ISRF), $F(z)$ is the local FUV photon flux computed over the same range of wavelength and α is the photodissociation rate for an unshielded ISRF. Note that even if this method seems to be crude, the non-trivial FUV attenuation by the dust-free gas prevents us from relying on more sophisticated fits as a function of N_{H} as used in typical dusty PDR models.

In order to avoid a prohibitive fine sampling of the radiation field around each UV line, CO and H_2 photodissociation are not treated according to the latter method. For CO photodissociation, we include self-shielding, and shielding by H_2 and by continuous process by expressing the photodissociation rate k_{CO} as

$$k_{\text{CO}} = 2.06 \times 10^{-10} \text{ s}^{-1} \theta_1(N(\text{CO})) \theta_2(N(\text{H}_2)) \frac{\chi}{1.23}, \quad (3)$$

where $\theta_1(N(\text{CO}))$ and $\theta_2(N(\text{H}_2))$ are self-shielding and cross-shielding factors tabulated by Lee et al. (1996) and χ is the ratio at 100 nm of the local FUV flux to the mean interstellar radiation field of Draine (1978) ($2 \times 10^{-6} \text{ erg s}^{-1} \text{ cm}^{-2} \text{ \AA}^{-1}$). The adopted shielding function gives a good approximation of the photodissociation rate of CO though neglecting the effect of the excitation of CO (Visser et al. 2009). Note that the factor 1.23 stands for the ratio between Mathis et al. (1983) and Draine (1978) UV flux at 100 nm. The photodissociation rate of H_2 is computed under the FGK approximation (Federman et al. 1979).

2.3. The excitation of H_2

Time-dependent populations of the first 50 ro-vibrational levels of H_2 in the electronic ground state are computed, including de-excitation by collision with H, He, H_2 and H^+ (Flower et al. 2003), UV radiative pumping of electronic lines followed by fluorescence (Godard et al. 2019), and excitation of H_2 due to formation on grain surfaces. For H_2 formation on grain surface, we assume that the levels are populated following a Boltzmann distribution at a temperature of $1/3$ of the dissociation energy of

Table 1. Elemental abundances adopted in dust-free and dusty models. The last two columns give the distribution of elemental abundances for a standard dust-to-gas ratio $Q_{\text{ref}} \equiv 6 \times 10^{-3}$. For dusty models with different dust-to-gas ratio, total elemental abundances are kept constant and elemental abundances in the grains are reduced by the same factor. Total elemental abundances and the elemental abundance in the grains are taken from Flower & Pineau des Forêts (2003) where carbon and hydrogen locked in PAH are assumed to be released in gas-phase for all model. Numbers in parentheses are powers of 10.

Element	$Q = 0$ (dust-free)	$Q = Q_{\text{ref}} \equiv 6 \times 10^{-3}$	
	Gas	Gas	Grain
H	1.00	1.00	0.00
He	1.00(-1)	1.00(-1)	0.00
C	3.55(-4)	1.92(-4)	1.63(-4)
N	7.94(-5)	7.94(-5)	0.00
O	4.42(-4)	3.02(-4)	1.40(-4)
Mg	3.70(-5)	0.0	3.70(-5)
Si	3.67(-5)	3.03(-6)	3.37(-5)
S	1.86(-5)	1.86(-5)	0.00
Fe	3.23(-5)	1.50(-8)	3.23(-5)

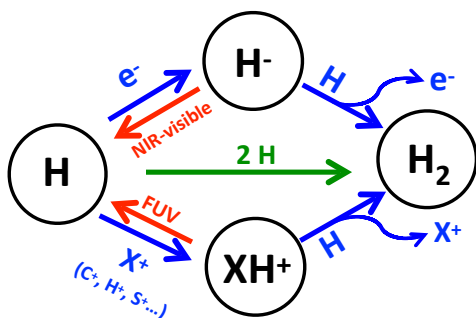


Fig. 2. Dust-free formation routes for H_2 where X stands for H, C, S, and Si. Blue arrows represent two-body reactions, the green arrow the three-body reaction and red arrows photodestruction of key intermediates.

H_2 (Black & van Dishoeck 1987). For H_2 gas-phase formation routes, levels are populated in proportion to their local population densities.

2.4. Elemental abundances

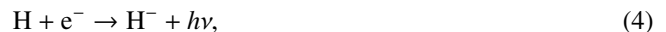
Total fractional elemental abundances are constructed from Table 1 of Flower & Pineau des Forêts (2003). For dust-free models, all elements are placed in the gas phase. For models with non-vanishing dust fraction, the dust content is quantified by the dust-to-gas mass ratio Q . The relative abundances between elements locked in the grains are assumed to be constant for any dust-to-gas ratio and equal to those of Flower & Pineau des Forêts (2003). PAHs are expected to be photodissociated by multi-photon events in the inner disk atmospheres (< 0.5 au, Visser et al. 2007). PAHs are consequently not included in the models and all carbon locked in PAHs is assumed to be released in gas phase. The resulting fractional elemental abundances are given in Table 1 for dust-free models and for dusty models with $Q = 6 \times 10^{-3}$. This value, which corresponds to a fractional abundance of grain of 6.9×10^{-11} (no sublimation of the grains), is taken as the reference for dusty models and we define $Q_{\text{ref}} \equiv 6 \times 10^{-3}$.

2.5. Chemical network

The chemical network is constructed from Flower & Pineau des Forêts (2015) and Godard et al. (2019). It includes 140 species and about a thousand gas-phase reactions. Details on the chemical reactions added to the former network, together with adopted rate coefficients, are given in Appendix B.

Regarding the formation of H_2 , three gas-phase formation routes are included (see Fig.2).

1. Electron catalysis through the intermediate anion H^- , via radiative attachment followed by fast associative detachment:



This route has been shown to be quenched due to the photodetachment of the fragile H^- by visible and NIR fields in T Tauri stellar winds (Rawlings et al. 1988; Glassgold et al. 1989) but efficient in the early universe at $z < 100$ (Galli & Palla 2013). We reconsider the role of this route in Section 3.

2. Ionic catalysis by any ion noted here X^+ (with $\text{X} = \text{H}, \text{C}, \text{S},$ and Si), through the intermediate ion XH^+ via radiative association followed by an ion-neutral reaction:



This route is very similar to the former though built from X^+ instead of e^- . In contrast with H^- , XH^+ ions are photodestroyed by UV photons and can thus survive the strong visible radiation fields. Surprisingly, previous models of dust-free stellar winds have never discussed formation routes via CH^+ , SiH^+ or SH^+ , focusing only on the formation route via H_2^+ . We show below and in Appendix C that the latter is inefficient compared to the formation by CH^+ or SiH^+ .

3. Three-body reaction:



that is relevant at high density.

Complementary reactions involved in the chemistry of the intermediates H_2^+ and H^- have also been included (see Appendix B).

Regarding H_2 formation on dust, we adopt the formation rate of Hollenbach & McKee (1979) assuming a single grain size distribution of radius a_g . An important caveat is the gas temperature dependence of the probability $S(T_K)$ that a H atom sticks when it collides with a grain. In the high temperature regime relevant for jets, large discrepancies exist in the literature regarding sticking probabilities, especially when including chemisorption or specific substrates (see Flower & Pineau des Forêts 2013, Appendix A). Our adopted expression for $S(T_K)$ (see eq. (C.24)) gives a lower limit on the formation rate of H_2 at high temperature.

In dust-poor gas, atomic species can dominate the opacity of the gas in the UV. When ionized, they can also contribute to the synthesis of the key anion H^- by increasing the electron fraction. Thus, a reduced chemical network for Mg/Mg^+ , incorporating photoionization and charge exchange reactions, has been added. Other rarer elements such as Li, Al or Na are not expected to contribute significantly in either the attenuation of the radiation field or the ionization balance of the gas and are consequently not included in the model.

Table 2. Physical parameters explored in single point models and their fiducial values.

Parameter	Symbol	Range or value	Fiducial
Density	n_H	$10^5 - 3 \times 10^{12} \text{ cm}^{-3}$	10^9 cm^{-3}
Temperature	T_K	200 - 5000 K	1000K
Dust fraction	Q/Q_{ref}	0 - 1	0
FUV field ^a	G_0	10^4	10^4
Visible field ^a	T_{vis}	4000 K	4000 K
Visible dilution ^a	W	5×10^{-7}	5×10^{-7}

^(a) The mean intensity of the radiation field is given by $J_\nu = WB_\nu(T_{\text{vis}}) + J_\nu^{FUV}$, where $B_\nu(T_{\text{vis}})$ is the intensity of a black-body radiation field at a temperature T_{vis} and J_ν^{FUV} the FUV part of the ISRF rescaled by G_0 (see Appendix A).

3. Chemistry

To examine the formation and destruction routes of the main molecules observed in protostellar jets, single spatial point models have been computed over a range of physical conditions representative of protostellar jets. The evolution of the gas is assumed to be isothermal and isochoric. Parameters of the models presented in this section are proton density n_H , kinetic temperature T_K , unshielded FUV radiation field G_0 and dilution factor of the (visible) black-body radiation field at 4000 K noted by W . The explored parameter space is summarized in Table 2. In this section, we discuss steady-state chemical abundances. This approach, though simple, allows us to identify relevant chemical reactions and capture the essential features of the chemistry operating in jets. The results of this section are summarized in Sec. 3.3.

3.1. Formation of H_2

Formation of H_2 constitutes the first step of molecular synthesis. The dominant gas-phase formation route of H_2 and its efficiency depends mainly on the ability of H^- to survive to photodetachment (see Fig. 2). The influence of dust on the chemistry depends then critically on the efficiency of gas-phase routes. Our results are summarized in Fig. 3 for specific values of $T_K = 1000 \text{ K}$, $x_e = 4.8 \times 10^{-4}$, and $x(C^+) = 3.6 \times 10^{-4}$. We first study H_2 formation in the absence of dust (bottom part of the Fig. 3 with boundaries ①, ②, and ③) and then the influence of a non-vanishing dust fraction (bulk of the diagram with boundaries ④, ⑤, ⑥, and ⑦). To generalize our results obtained here for a single set of values of T_K , G_0 and W , we also propose in Appendix C a numerically validated analytical approach that provides expressions for each boundary, and the associated formation rates of H_2 for any physical condition.

3.1.1. Dust-free

Figure 4 shows that in the absence of dust, and for a radiation field characterized by $G_0 = 10^4$ and $W = 5 \times 10^{-7}$, the gas remains atomic up to $n_H = 3 \times 10^{12} \text{ cm}^{-3}$. The abundance of H_2 increases from $\approx 10^{-9}$ up to ≈ 0.2 . Over the explored range of density, H_2 is preferentially photodissociated by the unshielded radiation field. Since the photodissociation rate does not depend on the density, the global trend seen in H_2 is mostly due to the formation routes.

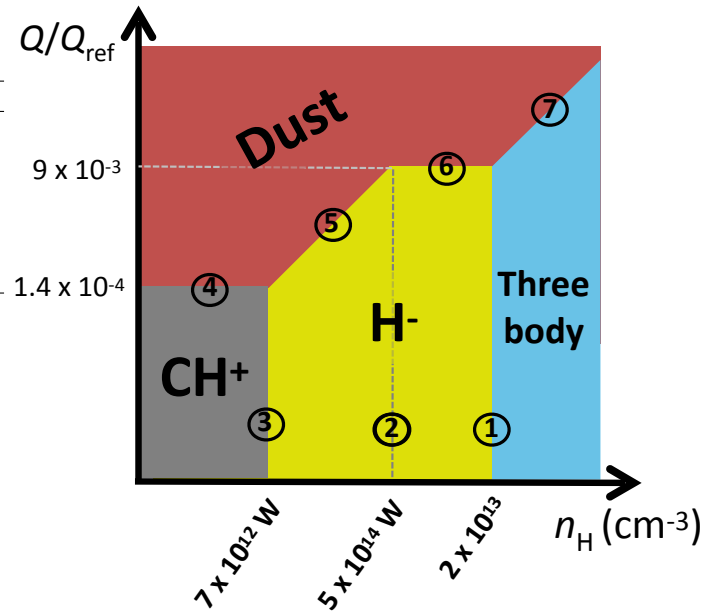


Fig. 3. Schematic view of the dominant H_2 formation routes depending on the density, the dust fraction and visible radiation field W summarizing our results presented in Section 3.1 and in Appendix C. The location of the boundaries are given for a temperature of $T_K = 1000 \text{ K}$, $x_e = 4.8 \times 10^{-4}$, and $x(C^+) = 3.6 \times 10^{-4}$. The schematic view remains valid from $\approx 100 \text{ K}$ up to $\approx 5000 \text{ K}$. Dependency on T_K , x_e , $x(C^+)$ are given in Appendix C. Note that some limits depend on the visible flux W and others do not. Depending on the visible flux, boundaries ①, ②, and ③ can merge.

We also plot an analytical model of the abundance of H_2 assuming formation by H^- only and destruction by photodissociation (see Appendix C, eq. (C.11)). The analytic expression reproduces very well the global increase of H_2 from $n_H = 3 \times 10^6$ to $3 \times 10^{11} \text{ cm}^{-3}$. In this regime, formation by H^- is the dominant formation route of H_2 (boundaries ③ to ①, Fig. 3). The route though H^- being a catalytic process by electrons, its efficiency depends linearly on the electron fraction. The recombination of ions at high density reduces the electron fraction and thus, the efficiency of this route. Below $n_H \approx 2 \times 10^8 \text{ cm}^{-3}$ (boundary ②), photodetachment of H^- takes over from the reaction $H^- + H \rightarrow H_2 + e^-$ leading to a decrease of H^- and limiting the formation rate of H_2 . Our analytical approach generalizes this result to any density and radiation field and shows that for a diluted black-body at 4000 K, this transition appears for (boundary ② and Appendix C, eq. (C.18))

$$\frac{n_H}{W} = 4.6 \times 10^{14} \text{ cm}^{-3}. \quad (9)$$

Despite the photodestruction of H^- , formation by H^- remains the dominant formation route of H_2 down to $n_H = 3 \times 10^6 \text{ cm}^{-3}$.

Below this value (boundary ③), the analytical model underestimates the H_2 abundance. In this regime, formation via CH^+ takes over from formation by H^- . This is due to a quenching of H^- route caused by a rapid photodetachment of H^- . For example, at the boundary ③, only $\sim 1\%$ of H^- formed by radiative attachment is actually converted in H_2 . More generally, this transition appears for (boundary ③, Appendix C, eq. (C.20))

$$n_H/W = 6.7 \times 10^{12} \text{ cm}^{-3} \left(\frac{x(C^+)}{3.6 \times 10^{-4}} \right) \left(\frac{x_e}{4.8 \times 10^{-4}} \right)^{-1} \left(\frac{T_K}{1000 \text{ K}} \right)^{-1.32}, \quad (10)$$

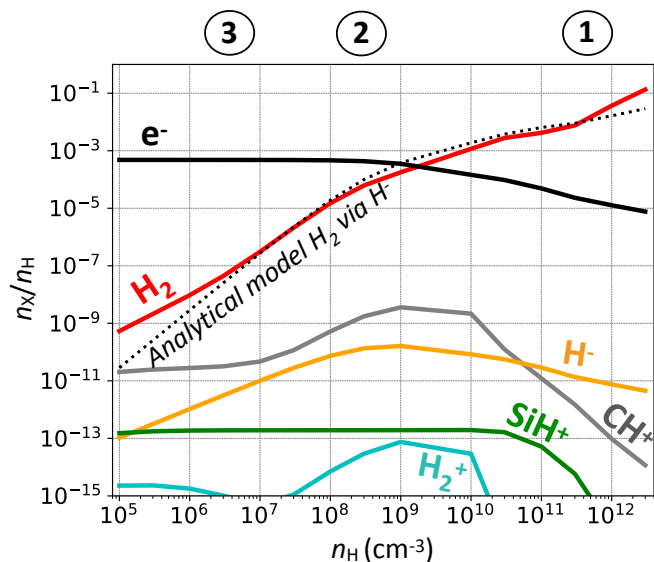


Fig. 4. Steady-state abundances relative to total H nuclei for H_2 and chemical species involved in its formation for dust-free single point models with $G_0 = 10^4$, $W = 5 \times 10^{-7}$, $T_K = 1000$ K, and n_{H} ranging from 10^5 to 2×10^{12} cm^{-3} . An analytical expression of the steady state abundance of H_2 assuming destruction by photodissociation and formation by H^- only is also plotted in black dotted line (see Appendix C). Boundaries defined in Fig. 3 are also indicated on the upper axis. Note that because of the decrease of the electron fraction following recombination at high density, three-body reaction takes over from the formation via H^- (boundary ①) at a lower density than indicated in Fig. 3.

where $x(\text{C}^+)$ is the abundance of C^+ . Interestingly, the very low radiative association rate of S^+ with H prevents this already rare element to participate significantly to the formation of H_2 via SH^+ . Formation via H_2^+ is found to be negligible over the explored parameter range. As seen in Fig. 4, H_2^+ is always at least two orders of magnitude less abundant than H^- , CH^+ or SiH^+ and does not form H_2 at similar levels.

Above $n_{\text{H}} = 3 \times 10^{11}$ cm^{-3} , the analytic model also underestimates the abundance of H_2 . In this regime, the three-body reaction route takes over from the formation by H^- . When H^- is not photodetached, this transition appears for (boundary ① and Appendix C, eq. (C.22))

$$n_{\text{H}} = 1.9 \times 10^{13} \text{ cm}^{-3} \left(\frac{x_e}{4.8 \cdot 10^{-4}} \right) \left(\frac{T_K}{1000 \text{ K}} \right)^{1.24}. \quad (11)$$

3.1.2. Dust-poor

Since these local models assume no attenuating material to the source, the inclusion of dust does not affect significantly the efficiency of gas-phase formation routes of H_2 . Consequently, our previous results on dust-free chemistry still hold. The effect of increasing dust fraction Q/Q_{ref} is to add a new formation route that can compete with gas-phase formation routes. The critical amount of dust above which formation on dust grain takes over depends on the efficiency of the dust-free formation route. Figure 5 shows the variation of the abundance of H_2 as function of the dust fraction Q/Q_{ref} for the fiducial radiation field, and for $n_{\text{H}} = 10^{10}$ cm^{-3} and $n_{\text{H}} = 10^5$ cm^{-3} . As shown above, gas-phase formation routes are dominated by H^- in the first case and by CH^+ in the latter.

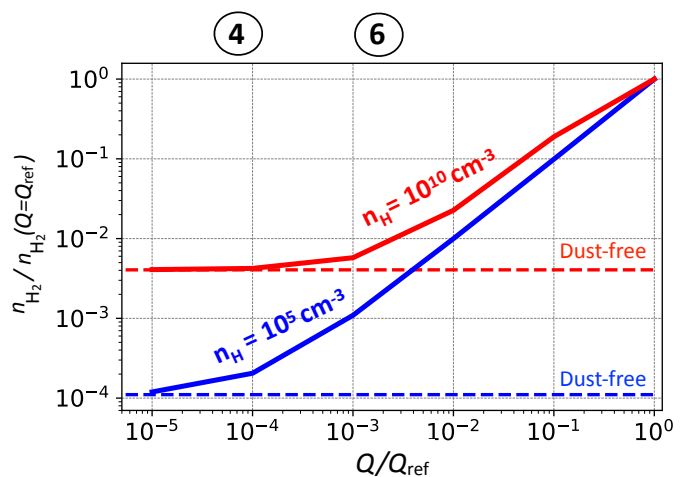


Fig. 5. Steady-state abundances of H_2 normalized to its value at $Q/Q_{\text{ref}} = 1$ as a function of Q/Q_{ref} for two densities : $n_{\text{H}} = 10^{10}$ cm^{-3} (solid red line) and $n_{\text{H}} = 10^5$ cm^{-3} (solid blue line). Other parameters are constant and equal to their fiducial values (see Table 2). Gas-phase formation of H_2 is dominated by H^- for $n_{\text{H}} = 10^{10}$ cm^{-3} ($n_{\text{H}}/W = 2 \times 10^{16}$ cm^{-3}) and by CH^+ for $n_{\text{H}} = 10^5$ cm^{-3} ($n_{\text{H}}/W = 2 \times 10^{11}$ cm^{-3}). Dashed lines indicate H_2 abundance in the absence of dust. Abundances for each set of model are normalized to their value at $Q/Q_{\text{ref}} = 1$. Note that because of the low electron fraction at $n_{\text{H}} = 10^{10}$ cm^{-3} ($x_e \approx 10^{-4}$) formation on grains takes over from the formation via H^- (boundary ⑥) at a lower dust fraction than indicated in Fig. 3.

Below $Q/Q_{\text{ref}} \approx 10^{-3}$ and for $n_{\text{H}} = 10^{10}$ cm^{-3} , the H_2 abundance is independent of the gas-to-dust ratio Q and equal to its dust-free value. In this regime, H_2 is formed through H^- with a maximal efficiency (H^- is not photodetached) and formation on dust is negligible. At about $Q/Q_{\text{ref}} \approx 2 \times 10^{-3}$ formation on dust takes over from gas-phase formation, driving up the H_2 abundance. A more detailed analysis (see Appendix C) shows that when H^- is the main formation route and not photodetached, the critical dust fraction below which H_2 gas-phase formation takes over from formation on grains is (Fig. 3, boundary ⑥)

$$Q/Q_{\text{ref}} = 9.3 \times 10^{-3} \left(\frac{T_K}{1000 \text{ K}} \right)^{0.4} \left(\frac{S(T_K)}{S(1000 \text{ K})} \right)^{-1} \left(\frac{x_e}{4.8 \cdot 10^{-4}} \right), \quad (12)$$

where $S(T_K)$ is the sticking coefficient of H on grains adopted from Hollenbach & McKee (1979). When the formation through H^- is reduced by photodetachment, this critical dust fraction is proportional to n_{H}/W (Fig. 3, boundary ⑤ and Appendix C eq. (C.25)).

Figure 5 shows that for a lower density-to-visible field ratio ($n_{\text{H}}/W = 2 \times 10^{11}$ cm^{-3}) dust has a significant impact at a much smaller dust fraction. As seen in the previous section, the gas-phase formation of H_2 is then dominated by CH^+ . Formation by CH^+ being about two orders of magnitude less efficient than electron catalysis, the critical dust fraction above which formation on grains takes over from gas-phase formation is accordingly lowered by a similar factor (Fig. 3, boundary ④ and Appendix C eq. (C.26)).

3.2. Other molecules

H_2 , even when scarce, constitutes the precursor of other molecules such as CO, SiO, OH, and H_2O that are observed

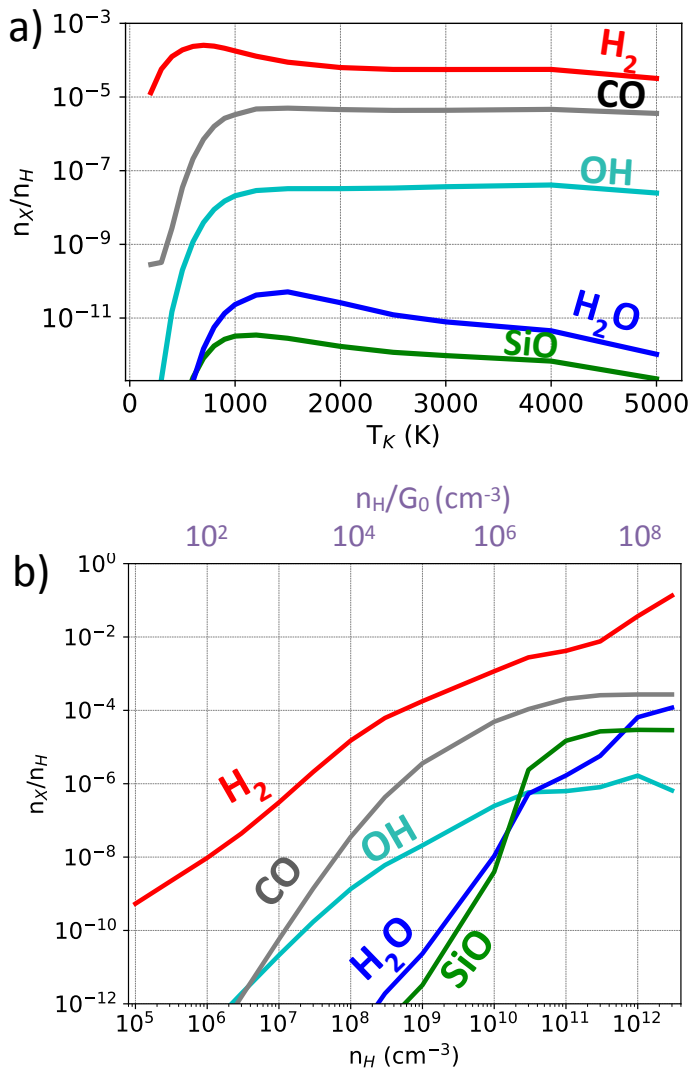


Fig. 6. Steady-state abundances relative to total H nuclei for relevant molecular species from single point models in the absence of dust. a) Abundances as function of temperature for $G_0 = 10^4$, $W = 5 \times 10^{-7}$, and $n_H = 10^9 \text{ cm}^{-3}$, b) abundances as function of n_H (lower axis) and n_H/G_0 (upper axis) for $T_K = 1000 \text{ K}$, $G_0 = 10^4$, and $W = 5 \times 10^{-7}$.

in protostellar jets. The molecular richness depends then on the abundance of H_2 . As such, the inclusion of dust increases molecular abundances only by increasing the fraction of H_2 . However, other physical variables can regulate molecular abundances such as the temperature, the FUV radiation field and the density. Since molecules are essentially formed by two-body reactions and destroyed by photodissociation in the UV domain, molecular abundances depends mostly on the ratio n_H/G_0 . In this section, results on molecular abundances obtained by varying n_H for fixed $G_0 = 10^4$ can thus be generalized for any G_0 by translating to the ratio n_H/G_0 .

3.2.1. Dust-free

Figure 6-a shows that steady-state abundances of OH, CO, H_2O and SiO increase by several orders of magnitude with temperature and reach maximum abundances above $\approx 1000 \text{ K}$. This trend is due to the activation of endothermic gas-phase forma-

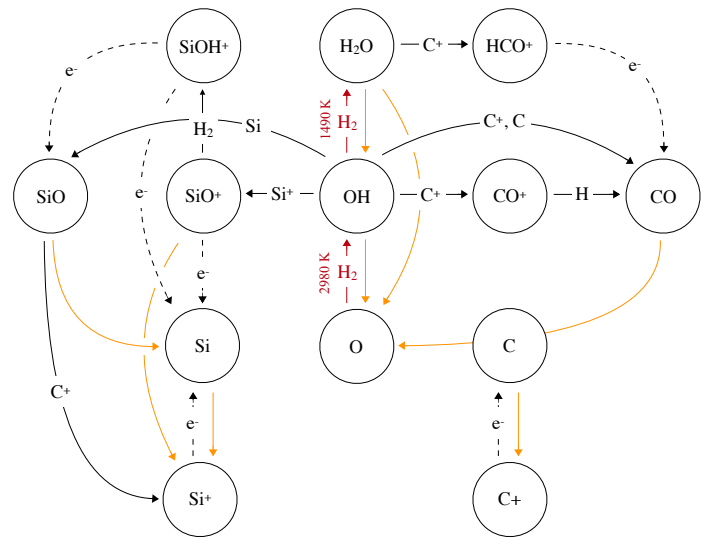
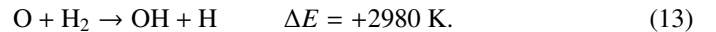


Fig. 7. Dominant reactions controlling the abundance of CO, H_2O , and SiO under warm ($T_K \geq 800 \text{ K}$) and irradiated conditions. OH appears to be a key intermediate for the three species. The ionization state of carbon controls the destruction of SiO and H_2O , and the formation of CO. The ionization state of silicon controls the formation of SiO. For unshielded ISRF FUV radiation field, carbon and silicon are ionized for $n_H/G_0 \leq 10^5 \text{ cm}^{-3}$ and $n_H/G_0 \leq 3 \times 10^6 \text{ cm}^{-3}$, respectively.

tion routes at high temperature. Formation of CO, SiO and H_2O is indeed initiated by the formation of OH through the neutral-neutral reaction



This warm route involving H_2 is fundamental for the formation of all the considered molecules, even if the H_2 fraction is low.

Figure 6-b shows steady-state abundances as function of density for a temperature of $T_K = 1000 \text{ K}$, sufficient for efficient molecule formation. As H_2 and OH increase with n_H , the abundances of the other species increase as well. For $n_H \geq 3 \times 10^{10} \text{ cm}^{-3}$, the gas is essentially atomic but rich in CO, SiO, H_2O . This is one of the most fundamental and unique characteristics of dust-free chemistry. Still, due to complex formation and destruction pathways, each molecular species behaves differently as a function of n_H , revealing their formation and destruction routes in H_2 poor gas. Figure 7 summarizes the dominant reactions contributing to the formation and destruction of CO, H_2O , SiO depending on the ionization state of C and Si.

The CO formation pathway is essentially regulated by the ionization state of the carbon. Below $n_H = 2 \times 10^9 \text{ cm}^{-3}$, carbon is ionized and CO is produced via the ion-neutral reaction $\text{C}^+ + \text{OH}$ producing either directly CO or CO^+ . In the latter, CO^+ is neutralised by a fast charge exchange with H. Above $n_H = 2 \times 10^9 \text{ cm}^{-3}$, CO is produced directly by the neutral-neutral reaction $\text{C} + \text{OH} \rightarrow \text{CO}$. Destruction is mostly via photodissociation.

The H_2O abundance exhibits a stiff increase with n_H . Over the explored parameter range, H_2O is produced through the neutral-neutral reaction $\text{OH} + \text{H}_2$. Below $n_H \approx 10^{10} \text{ cm}^{-3}$, destruction is via photodissociation, and by C^+ . At higher density, the main destruction route is via the reverse reaction $\text{H}_2\text{O} + \text{H} \rightarrow \text{OH} + \text{H}_2$.

The SiO abundance exhibits a stiff increase around $n_H \approx 3 \times 10^{10} \text{ cm}^{-3}$, rising by more than four orders of magnitudes

in one decade of n_{H} . This feature is due to a change in both destruction and formation routes. Below $n_{\text{H}} = 3 \times 10^{10} \text{ cm}^{-3}$, Si^+ is the main silicon carrier and SiO synthesis is initiated by the ion-neutral reaction $\text{Si}^+ + \text{OH} \rightarrow \text{SiO}^+$. However, in contrast to the analogous reaction with CO^+ , SiO^+ cannot be neutralized through a charge exchange with the main collider, namely H. Alternatively, SiO^+ decays toward SiO though $\text{SiO}^+ + \text{H}_2 \rightarrow \text{SiOH}^+$, eventually leading to SiO. H_2 being rare in the absence of dust, this formation route is much less efficient than the analogous reaction that forms CO. In addition, at low n_{H}/G_0 , the abundant C^+ destroys efficiently SiO to form CO. Consequently when carbon and silicon are ionized, the medium is hostile to the formation and the survival of SiO. On the contrary, above $n_{\text{H}} \approx 3 \times 10^{10} \text{ cm}^{-3}$, SiO is formed directly through the neutral-neutral reaction $\text{Si} + \text{OH}$ and destruction by C^+ is quenched by the recombination of carbon. In contrast with the analogous reaction with H_2O , the reverse reaction $\text{SiO} + \text{H}$ has a very high endothermicity (3.84 eV) that prevents any destruction by H. Given these favorable factors, SiO becomes the main silicon reservoir above $n_{\text{H}} \approx 3 \times 10^{10} \text{ cm}^{-3}$.

3.2.2. Dust-poor

The inclusion of dust increases the molecular abundances by increasing the H_2 abundance. Thus, the minimal amount of dust required to affect the chemistry of CO, OH, SiO, H_2O is similar to that determined in the Sec. 3.1.2. Molecular abundances are then increased accordingly but specific formation and destruction routes remain the same.

3.3. Summary

In this section, the chemistry of dust-free and dust-poor gas has been studied. Regarding H_2 , we show that the dominant gas-phase formation route and its efficiency depends critically on the ratio between the density and the visible radiation field, quantified here by n_{H}/W . Above $n_{\text{H}}/W \approx 5 \times 10^{14} \text{ cm}^{-3}$, H_2 is efficiently formed via H^- whereas below this value, photodetachment reduces its efficiency. When optimally formed via H^- , a minimum fraction of dust of about $Q/Q_{\text{ref}} \approx 2 \times 10^{-3}$ is required to have a significant impact on the chemistry.

Regarding CO, OH, SiO and H_2O , we find that high abundances are reached for $n_{\text{H}}/G_0 \geq 10^6 \text{ cm}^{-3}$, despite low abundances of H_2 . Efficient formation routes are initiated by OH and require a warm environment ($T_{\text{K}} \geq 800 \text{ K}$). The inclusion of dust increases molecular abundances by increasing the H_2 abundance accordingly. We also find that the abundance of SiO is very sensitive to the ionization state of carbon and silicon. When both species are singly ionized, the SiO abundance is very low due to both destruction by C^+ and a very low efficiency of the formation by Si^+ in an H_2 -poor environment.

4. 1D wind models

In this section, the chemistry studied in the previous section is incorporated in a more realistic model of 1D wind streamline. In addition to the quantities found to control the chemistry in unattenuated static environments (namely n_{H}/G_0 , n_{H}/W , T_{K} , Q/Q_{ref} , and T_{vis}), we include three ingredients: the attenuation of the radiation field with the distance from the source, the time-dependent chemistry, and the differential geometrical dilutions of the density and the radiation field. We present below our simple 1D model where these effects are implemented with a min-

imal number of free parameters, allowing to investigate a wide range of source evolutionary phases.

4.1. The streamline model

The disk wind model, illustrated in Figure 8-a, is built from a simple flow geometry that captures the essential properties of MHD disk wind models in a parametric approach, without relying on a peculiar wind solution. Following Kurosawa et al. (2006) we assume that the wind is launched from a region of the disk between R_{in} and R_{out} , and propagates along straight streamlines diverging from a point located at a distance $-z_0$ below the central object (Fig. 8-a).

We follow the evolution of only one representative streamline launched from R_0 using the astrochemical model presented in Section 2. To reduce the number of free parameters, the wind velocity, noted V_j , is assumed to be constant with distance. Conservation of mass then yields a geometrical dilution of density along the streamline anchored at R_0 of

$$n_{\text{H}}(z) = n_{\text{H}}^0 \frac{1}{\left(1 + \frac{z}{z_0}\right)^2}, \quad (14)$$

where we note n_{H}^0 the density at the base ($z = 0$).

The radiation field is assumed to be emitted isotropically from the star position. Along a given streamline, it is reduced by a geometrical dilution factor, and attenuated by gas-phase species and dust, if any. To keep the problem tractable in 1D, the attenuation of the radiation field is assumed to proceed along each streamline. The geometrically diluted, unattenuated FUV field at position z is given by

$$G_0(z) = G_0^0 \frac{1}{\left(1 + \frac{z}{z_0}\right)^2 + \left(\frac{z}{R_0}\right)^2}, \quad (15)$$

where we note G_0^0 the unattenuated FUV field at the base ($z = 0$). The same geometrical dilution applies to the unattenuated visible radiation field.

Figure 8-b,c show that under this simple wind geometry, the radiation field is diluted on a spatial scale $\approx R_0$ while the density field is diluted on a scale z_0 . Due to the collimation of the flow ($z_0 \gg R_0$), the ratios n_{H}/G_0 and n_{H}/W (which would determine the flow chemistry in the absence of attenuation and time-dependent effects) increase with distance up to a factor $1 + (z_0/R_0)^2$ from their initial values at $z = 0$. Hence, the differential dilutions of the radiation and density fields in our model is regulated by the wind collimation angle (z_0/R_0).

Our 1D chemical wind-model is thus controlled in principle by 9 free parameters: the same six parameters as in Section 3, namely n_{H}^0 , G_0^0 , W^0 , T_{K} , Q/Q_{ref} , and T_{vis} ; and three parameters controlling the wind attenuation, dilution, and non-equilibrium effects: the opening angle of the streamline z_0/R_0 , the typical attenuation scale z_0 (or alternatively the anchor radius R_0), and the velocity of the wind V_j . Since we cannot explore the full parameter space in the present study, we chose here to fix most of them to representative values observed in molecular jets and young protostars, and focus on varying the source evolutionary status. Namely, we take a fixed launch radius $R_0 = 0.15 \text{ au}$ (as estimated for the SiO jet in HH 212 by Tabone et al. 2017). The ratio z_0/R_0 is fixed to 25, leading to an opening angle of the computed streamline of 5° , in line with the observed universal collimation properties of jets across ages (Cabrit 2007a; Cabrit et al. 2007). The wind velocity V_j is taken equal to 100 km s^{-1} , in line with

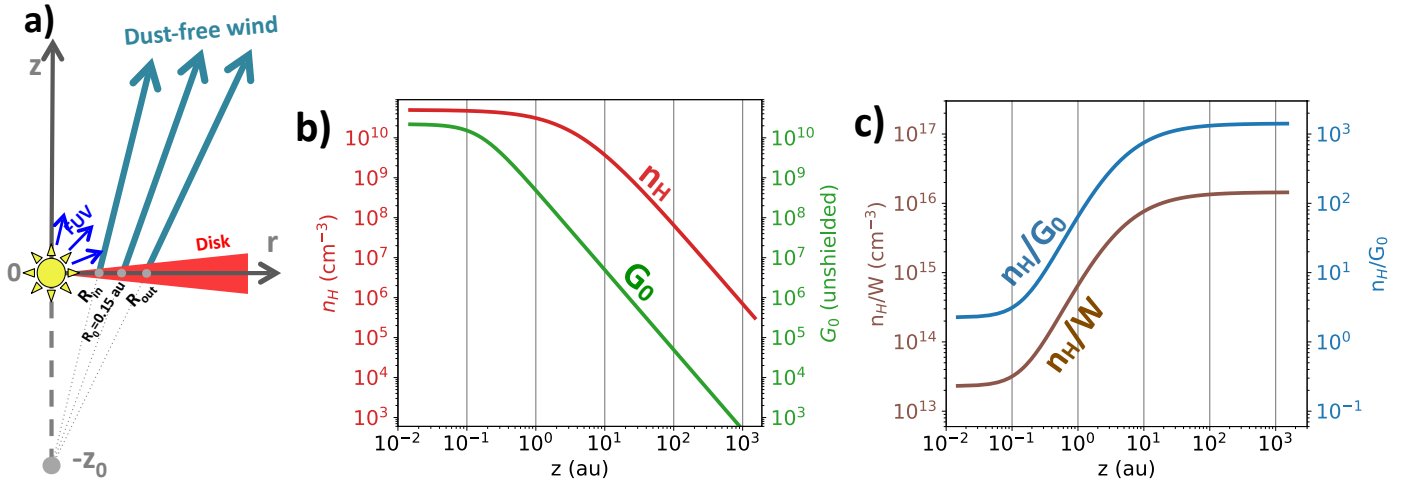


Fig. 8. Wind model adopted in this work. a) Schematic view of the geometry of the model. Streamlines are assumed to be straight lines launched from the disk (see Fig. 1-a). The wind velocity V_j is constant and equal to 100 km s^{-1} . The wind launching region extends from $R_{\text{in}} = 0.05 \text{ au}$ out to $R_{\text{out}} = 0.3 \text{ au}$. We focus on the chemical evolution of a representative streamline launched from 0.15 au in the disk and reduce the problem to 1D (see Sec. 4.1). b) Prescribed density n_{H} and unshielded FUV flux G_0 profile along the representative streamline launched from 0.15 au for wind solution @ (see Table 3). For other models, n_{H} and G_0 are simply rescaled according to the eqs. (19) and (17), respectively. c) Prescribed n_{H}/G_0 and n_{H}/W ratio along the same streamline. Note that due to the collimation of the flow ($z_0 \gg R_0$), these ratios are increasing with distance by a factor $(z_0/R_0)^2 = 625$. In the absence of dust, the opacity of the gas in the visible is negligible so that n_{H}/W ratio is expected to be the true local ratio between density and visible field.

Table 3. Models explored in this work in order of increasing source age.

Model	label	M_* M_{\odot}	\dot{M}_{acc} $M_{\odot} \text{ yr}^{-1}$	\dot{M}_{w} $M_{\odot} \text{ yr}^{-1}$	n_{H}^0 cm^{-3}	G_0^0	n_{H}^0/G_0^0 cm^{-3}	n_{H}^0/W^0 cm^{-3}
Class 0	Ⓐ	0.1	5(-5)	5(-6)	1.3(11)	5.5(10)	2.4	5.9(13)
		0.1	2(-5)	2(-6)	5.0(10)	2.2(10)	2.3	2.3(13)
	Ⓑ	0.1	1(-5)	1(-6)	2.5(10)	1.1(10)	2.3	1.1(13)
		0.1	5(-6)	5(-7)	1.3(10)	5.5(09)	2.4	5.9(12)
Class I	Ⓒ	0.5	1(-6)	1(-7)	2.5(09)	5.5(09)	0.45	1.1(12)
Class II		0.5	1(-7)	1(-8)	2.5(08)	5.5(08)	0.45	1.1(11)

Notes. Except for M_* and \dot{M}_{w} , all parameters have fixed values, namely $R_* = 3 R_{\odot}$, $T_{\text{vis}} = 4000 \text{ K}$, $V_j = 100 \text{ km s}^{-1}$, $T_{\text{K}} = 1000 \text{ K}$, $R_{\text{in}} = 0.05 \text{ au}$, $R_{\text{out}} = 0.3 \text{ au}$, $R_0 = 0.15 \text{ au}$, and $z_0/R_0 = 25$. Accretion to ejection rate ratio is assumed to be 0.1 so that $\dot{M}_{\text{w}} = 0.1\dot{M}_{\text{acc}}$ for all models. Models in bold are studied in more details in section 4.2 (see also Fig. 9), and are identified by a label. The last four columns are the density, the FUV radiation field, and the ratios n_{H}^0/G_0^0 , and n_{H}^0/W^0 at the base of the computed streamline. Numbers in parentheses are powers of 10.

typical velocities measured from proper motions toward Class 0 molecular jets (eg. Lee et al. 2015). The flow temperature is taken as $T_{\text{K}} = 1000 \text{ K}$ (see discussion in Section 5.2).

The radiation field emitted by the accreting protostar is modelled as a black-body of photospheric origin with $T_{\text{vis}} = 4000 \text{ K}$, plus a FUV component coming from the accretion shock onto the stellar surface. At the base of the streamline, the dilution factor of the stellar black-body, defined as $W \equiv \frac{J_{\nu}}{B_{\nu}}$, is (assuming $R_0 \gg R_*$)

$$W^0 = \frac{1}{4} \left(\frac{R_*}{R_0} \right)^2 = 2.2 \cdot 10^{-3} \left(\frac{R_0}{0.15 \text{ au}} \right)^{-2} \left(\frac{R_*}{3R_{\odot}} \right)^2. \quad (16)$$

The radius of the protostar is fixed to $R_* = 3R_{\odot}$, with R_{\odot} the solar radius. Regarding UV excess, FUV observations of BP Tau and TW Hya show that an ISRF provides a good proxy for the shape of the radiation field, though neglecting the line contribution to the FUV flux ($> 35\%$, Bergin et al. 2003). Here, we assume that the FUV excess follows a Mathis radiation field (Mathis et al. 1983, see appendix A) and neglect the UV line emission. For BP Tau, Bergin et al. (2003) find that a FUV flux of $G_0 = 560$ at 100 au is required to match the FUV continuum level. Assuming

that the FUV flux scales with the accretion luminosity $L_{\text{acc}} = \frac{GM_*\dot{M}_{\text{acc}}}{R_*}$ (which is $0.24L_{\odot}$ for BP Tau), the scaling factor at the base of the streamline anchored at R_0 is

$$G_0^0 = 1.1 \times 10^{10} \left(\frac{\dot{M}_{\text{acc}}}{10^{-5} M_{\odot} \text{ yr}^{-1}} \right) \left(\frac{M_*}{0.1 M_{\odot}} \right) \left(\frac{R_*}{3R_{\odot}} \right)^{-1} \left(\frac{R_0}{0.15 \text{ au}} \right)^{-2}, \quad (17)$$

where \dot{M}_{acc} is the accretion rate onto the protostar and M_* is the mass of the protostar.

In order to relate the density at the launching point of a streamline n_{H}^0 to the mass-loss rate of the wind \dot{M}_{w} , we assume that between R_{in} and R_{out} , the wind has a constant local mass-loss rate. This gives a density structure at the base of the wind of

$$n_{\text{H}}^0 = \frac{0.5\dot{M}_{\text{w}}}{2\pi \cdot 1.4 m_{\text{H}} V_j R_0 (R_{\text{out}} - R_{\text{in}})}, \quad (18)$$

where \dot{M}_{w} is the (two-sided) mass-loss rate of the wind. Note that for winds launched from a narrow region of the disk ($R_{\text{out}} \approx$

few R_{in}), the choice of the power-law index of the local mass-loss rate has a weak influence on n_{H}^0 . In this work, we follow the modeling results of the SiO jet in HH212 (Tabone et al. 2017) and we fix $R_{\text{in}} = 0.05$ au and $R_{\text{out}} = 0.3$ au, leading to a density at the base of the streamlines of

$$n_{\text{H}}^0 = 2.5 \times 10^{10} \frac{\dot{M}_{\text{w}}}{10^{-6} M_{\odot} \text{ yr}^{-1}} \left(\frac{0.25 \text{ au}}{R_{\text{out}} - R_{\text{in}}} \right) \left(\frac{V_{\text{j}}}{100 \text{ km s}^{-1}} \right)^{-1} \left(\frac{0.15 \text{ au}}{R_0} \right) \text{ cm}^{-3}. \quad (19)$$

To further reduce the parameter space, we follow the universal correlation between accretion and ejection observed from Class 0 to Class II jets and set the (two-sided) wind mass-flux to $\dot{M}_{\text{w}} = 0.1 \dot{M}_{\text{acc}}$.

In the end, the parameter space in the present study is thus reduced to only three free parameters: \dot{M}_{acc} , M_{\star} , and Q/Q_{ref} . To investigate how the chemical content of a dust poor, laminar jet evolves in time with the decline of accretion rate and the increase in stellar mass we computed six sets of wind model summarized in Table 3, namely

1. Four models of a Class 0 wind. At this stage, the young embedded source has not reached its final mass yet and we choose $M_{\star} = 0.1 M_{\odot}$. Accretion rate is varied from $\dot{M}_{\text{acc}} = 5 \times 10^{-5} M_{\odot} \text{ yr}^{-1}$ to $5 \times 10^{-6} M_{\odot} \text{ yr}^{-1}$ to model sources with various accretion luminosities.
2. A model of a Class I wind. At this stage, the protostar has accumulated most of its mass and we choose $M_{\star} = 0.5 M_{\odot}$ with an accretion rate of $\dot{M}_{\text{acc}} = 10^{-6} M_{\odot} \text{ yr}^{-1}$.
3. A model of a Class II wind with an accretion rate of $\dot{M}_{\text{acc}} = 10^{-7} M_{\odot} \text{ yr}^{-1}$ and $M_{\star} = 0.5 M_{\odot}$. This accretion rate is representative for actively accreting T Tauri star.

To study the impact of surviving dust, the five wind models have been computed for dust fraction $Q/Q_{\text{ref}} = 0, 10^{-3}, 10^{-2},$ and 0.1 .

The initial chemical abundances at the base of the streamline are computed as in Section 3, i.e. assuming chemical equilibrium and no attenuation of the radiation field. Hence they depend only on the adopted $T_{\text{K}} = 1000$ K, $T_{\text{vis}} = 4000$ K, and the initial ratios n_{H}^0/G_0^0 and n_{H}^0/W_0^0 given in Table 3 for all models.

4.2. Results: dust-free winds

In this section, we present results on dust-free wind models ($Q = 0$). Chemical abundances and local FUV radiation field of the selected wind models ④, ⑤ and ⑥ (see Table 3) are presented in Fig. 9. These specific models allow to highlight the influence of the wind parameters, namely the density of the wind (e.g mass-loss rate) and the radiation field. Models ④ and ⑤ have a different n_{H} and G_0 but share the same n_{H}/G_0 ratio. Models ⑤ and ⑥ have a similar FUV radiation field but a different density (Table 3). Asymptotic abundances for the full set of dust-free wind models are also given in Fig. 10 (solid line).

4.2.1. FUV field

One of the main difference between single point models and wind models is the inclusion of the attenuation of the radiation field along streamlines. In dust-free winds, only gas-phase species can shield the radiation field and decrease photodissociation rates of molecular species.

Figure 9 (right panels) shows that the attenuation of the radiation field results in sharp absorption patterns characterized by

thresholds below which the radiation field is heavily extinguished. Those thresholds correspond to ionization thresholds of the most abundant atomic species. This specific attenuation pattern has already been pointed out by Glassgold et al. (1989, 1991) in the context of stellar winds, although without focusing on the sharpness of the attenuation patterns that is at the root of the chemical richness of dust-free jets. The specific shielding mechanism that causes these unique attenuation patterns can be understood by the inspection the model ⑥ (Fig. 9-b). In the absence of attenuation, carbon is expected to be ionized. However, at $z \simeq 2$ au, the abundance of C^+ drops by several orders of magnitude (right panel) and neutral carbon (not shown here) becomes the main carbon carrier. Figure 9-b, right panel, shows that above this transition, photons below the photoionization threshold of carbon ($\lambda \leq 1100$ Å) are attenuated by more than 8 orders of magnitude. In this region of the spectrum, the opacity of the gas is dominated by carbon. The steep decrease of C^+ is thus due to the attenuation by carbon itself, triggering a C^+/C transition when the gas becomes optically thick to ionizing photons. Because of the increase of C at the C^+/C transition, the local opacity of the gas increases even more. This leads to an attenuation of the FUV field below $\lambda = 1100$ Å that is much stiffer than attenuation by dust. This process, called continuum self-shielding and included in most of the dusty PDR models (Röllig et al. 2007), turns to be of paramount importance in dust-free and dust-poor winds.

The resulting attenuation of the FUV radiation field is very sensitive to the wind model. For model ④, with a higher mass-loss rate, the radiation field at $z = 1000$ au is strongly attenuated down to the ionization wavelength threshold of sulfur, which has a relatively large value ($\lambda = 1600$ Å), whereas for model ⑥, with a lower mass-loss rate, the radiation field is barely extinguished across the FUV spectrum. As any self-shielding process, it depends on the column density of the neutral atom X. In the inner ionized and unattenuated part of the jet, this column density increases with z as

$$N_{\text{X}}(z) = n_{\text{X}}^0 z_0 \int_0^{z/z_0} \frac{(1+u)^2 + (\frac{z_0}{R_0} u)^2}{(1+u)^4} du \quad (20)$$

where n_{X}^0 is the density of X at the launching point and is proportional to $(n_{\text{H}}^0)^2/G_0^0$. The self shielding occurs if $N_{\text{X}}(z)$ becomes typically larger than σ_{X}^{-1} where σ_{X} is the FUV absorption cross section⁴ of atom X. Because the integral term on the right hand side converges, eq. 20 reveals a threshold effect: if $(n_{\text{H}}^0)^2/G_0^0$ is too low, $N_{\text{X}}(z)$ is found to never rise above the critical value required to trigger the self-shielding, regardless of z .

Models ④ and ⑤ share the same unshielded n_{H}^0/G_0^0 ratio and consequently exhibit similar atomic abundances at the base of the wind. However, model ④ being denser, its $(n_{\text{H}}^0)^2/G_0^0$ ratio is larger. This increases the total column density of S and Si which exhibit self-shielding transitions. This results in attenuation of the radiation field at much longer wavelengths. In contrast, model ⑥ having both a lower n_{H}^0/G_0^0 ratio and a lower density, the column density of carbon is not sufficient to attenuate the radiation field and the shape of the radiation field remains unaltered.

In other words, in the absence of dust, the radiation field is attenuated by continuum self-shielding of atoms. This process is very efficient at attenuating the radiation field below the photoionization thresholds of the atomic species. The wavelength below which the radiation field is attenuated depends on

⁴ The FUV absorption cross sections of C, S, and Si are of the order of a few 10^{-17} cm^2 .

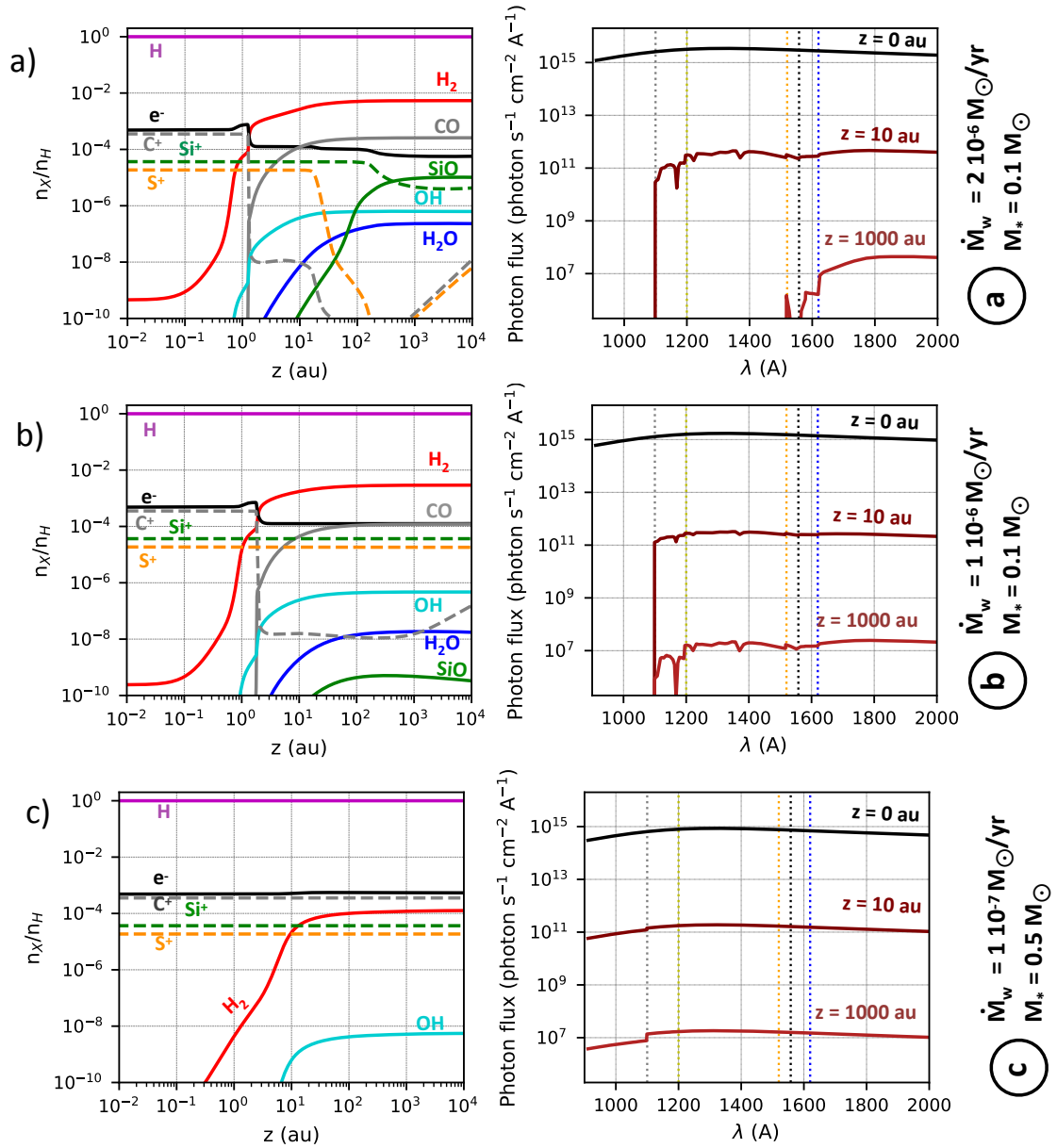


Fig. 9. Computed chemical abundances and local FUV radiation field for dust-free isothermal wind models for $T_K = 1000$ K. Left panels: chemical abundances relative to total H nuclei. Right panels: local mean intensity of the FUV radiation field at various position along the wind (position indicated on the curves). Photoionization thresholds of C, S, Si, Mg, and Fe are also indicated by gray, yellow, orange, black and blue dashed lines respectively. a) Class 0 model with $\dot{M}_w = 2 \times 10^{-6} M_\odot \text{ yr}^{-1}$ and $M_* = 0.1 M_\odot$. b) Class 0 model with a lower mass-loss rate $\dot{M}_w = 10^{-6} M_\odot \text{ yr}^{-1}$ and same mass. c) Class I model, with lower accretion rate $\dot{M}_w = 10^{-7} M_\odot \text{ yr}^{-1}$ but higher mass $M_* = 0.5 M_\odot$.

the species that are self-shielded. Carbon can attenuate radiation field at short wavelength whereas S, Si attenuate the radiation field at longer wavelength. Self-shielding by a specific species is very sensitive to the density of the wind. It results that Class II and I models are not dense enough to be shielded by any atom whereas Class 0 models are shielded by carbon for $\dot{M}_w \geq 5 \times 10^{-7} M_\odot \text{ yr}^{-1}$ and by carbon, silicon and sulfur for $\dot{M}_w \geq 2 \times 10^{-6} M_\odot \text{ yr}^{-1}$.

4.2.2. H_2

Figure 9 (left panels) and Fig. 10 show that dust-free wind models are poor in H_2 and consequently mostly atomic. H_2 is also smoothly increasing with increasing mass-loss rate. For Class 0 wind models, typical values of 10^{-3} are found above $z = 10$ au.

This global trend with mass-loss rate is due to both an increase in the formation efficiency, and a decrease in destruction efficiency.

Regarding formation pathways, formation of H_2 is dominated by H^- for all models, except at the base of the wind where H_2 is formed by CH^+ in Class I and II models. As seen in Section 3, the efficiency of the H^- route depends on the ratio n_{H}/W , that quantifies the ability of H^- to form H_2 instead of being photodestroyed by the visible field. All models share the same visible radiation field so that the ratio n_{H}/W depends only on the density of the wind (i.e. mass-loss rate). Consequently, the efficiency of the formation of H_2 by H^- increases progressively with the mass-loss rate.

Along with the increase of the formation efficiency, the destruction efficiency decreases with mass-loss rate. For Class II models, destruction of H_2 are dominated by photodissociation.

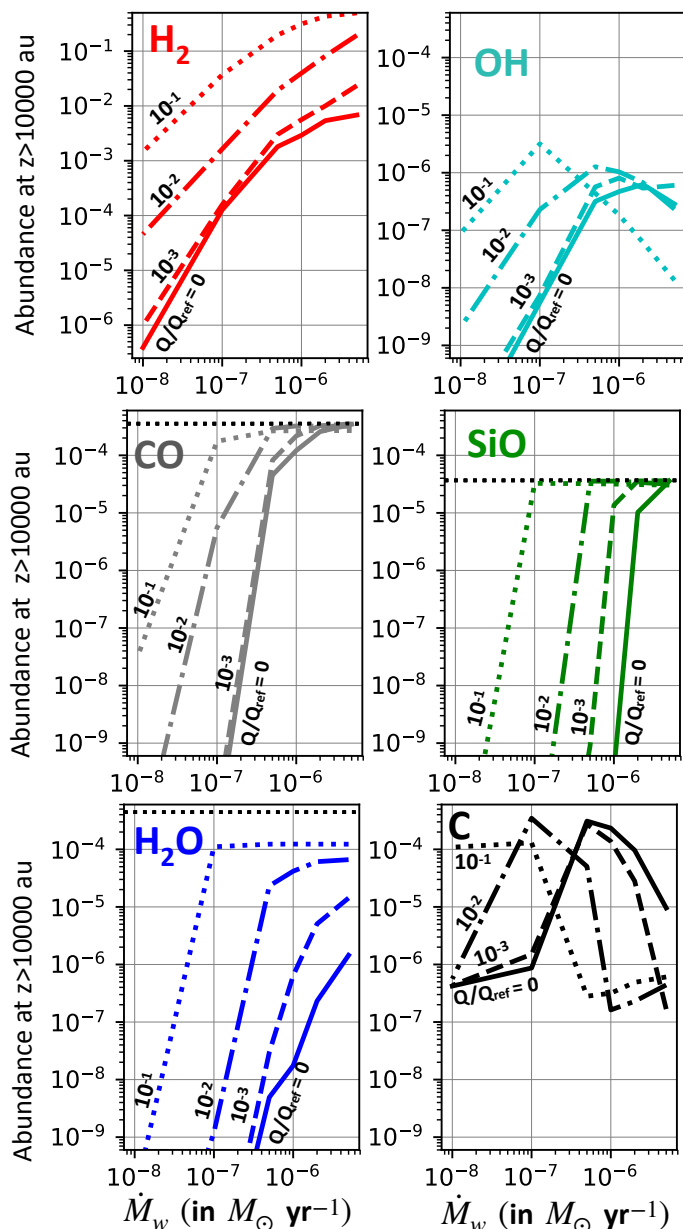


Fig. 10. Abundances at $z > 10000$ au for a streamline anchored at 0.15 au in the disk as function of the mass-loss rate for various dust fraction. For $\dot{M}_w \geq 5 \times 10^{-7} M_\odot \text{ yr}^{-1}$, the mass of the central object is $0.1 M_\odot$ (Class 0 model) and $0.5 M_\odot$ for lower mass-loss rates (Class I and II models). Dust-free models are plotted in solid lines, and dust-poor models with $Q/Q_{\text{ref}} = 10^{-3}$, 10^{-2} and 0.1 are plotted in dashed, dashed-dotted and dotted lines, respectively as indicated in each panel. Horizontal black dotted lines indicate the elemental abundance of carbon (panel on CO), silicon (panel on SiO), and oxygen (panel on H_2O).

Class I models exhibit sufficiently high column density of H_2 to insure an efficient self-shielding, quenching photodissociation route. Alternatively, destruction by C^+ according to $\text{C}^+ + \text{H}_2 \rightarrow \text{CH}^+ \rightarrow \text{C}^+ + \text{H}$ takes over from photodissociation with a smaller efficiency. For even larger mass-loss rates, the self-shielding of atomic carbon leads to a drop of C^+ , quenching the former destruction route. Alternatively, H_2 is destroyed by atomic oxygen according to $\text{O} + \text{H}_2 \rightarrow \text{OH} \rightarrow \text{O} + \text{H}$.

In other words, dust-free wind models are mostly atomic. The H_2 abundance increases with mass-loss rate due to an increase of the efficiency of the formation route by H^- and a de-

crease of the destruction route with the progressive self-shielding of H_2 and the recombination of C^+ .

4.2.3. Other molecules

Figure 10 shows that along with the increase of H_2 with the accretion rate, molecular abundances of interest increase with the mass-loss rate. As shown in Section 3, H_2 abundance regulates the formation of OH, CO, SiO and H_2O . On the other hand, continuum self-shielding of atomic species is a crucial process for the survival of these molecules: it reduces photodissociation rates by attenuating the FUV radiation field and quenches destruction routes by C^+ . However, the precise impact of the shielding by atoms depends on the photodissociation threshold of each molecular species relative to the threshold below which the radiation field is attenuated.

OH is the first neutral species to be formed after H_2 , and is an important intermediate for the synthesis of other molecules. Figure 10 shows that OH abundance is found to increase smoothly with mass-loss rate following the increase in H_2 abundance. Its abundance remains low, reaching 6×10^{-7} for model @. The wavelength dissociation threshold of OH being larger than the ionization thresholds of C, S, Si, Fe, and Mg, OH is not efficiently shielded by those species. Consequently, OH is destroyed by photodissociation at all \dot{M}_w and the increase of OH with \dot{M}_w is mostly driven by the smooth increase of H_2 and the increase of formation rates with density. Interestingly, at the highest mass-loss rate, the abundance of OH is also limited by the reverse reaction $\text{OH} + \text{H} \rightarrow \text{O} + \text{H}_2$.

CO is found to exhibit a much steeper increase with \dot{M}_w from Class II-I models to Class 0 models (Fig. 10). For Class 0 models, the CO abundance is high at $\geq 10^{-5}$. Interestingly, the abundance ratio CO/H_2 is $\approx 2 - 5 \times 10^{-2}$ in Class 0 models. This value is much larger than the canonical value derived in dusty molecular gas ($\approx 10^{-4}$) and constitutes one of the most striking characteristics of dust-free jets. The global behavior of CO is related to the shielding mechanism of the wind by carbon. In contrast with OH, the CO wavelength dissociation threshold lays below the wavelength ionization threshold of carbon. CO can thus be efficiently shielded by carbon, when the column density of C is sufficient to trigger self-shielding of C. This process is notable in both Class 0 models presented in Fig. 9 where a jump in CO by several orders of magnitude is seen across the C/C^+ transition. Since self-shielding of carbon is only operating in Class 0, CO is abundant only in dust-free Class 0 models.

SiO exhibits an even steeper increase with mass-loss rate and is abundant only for the highest mass-loss rates ($\dot{M}_w \geq 2 \times 10^{-7} M_\odot \text{ yr}^{-1}$). Such a high sensitivity of SiO to the mass-loss rate is related to the self-shielding of silicon that ultimately controls formation and destruction of SiO. Regarding destruction, SiO has an intermediate wavelength dissociation thresholds ($\lambda_{th} = 1500 \text{ \AA}$) that lies between C and Si ionization thresholds. As for OH, shielding by C does not reduce significantly photodissociation rates but in contrast to OH, shielding by S and Si is very efficient. As a consequence, the SiO photodissociation rate falls from model @ to model @. Regarding formation routes, as shown in Sec. 3 and Fig. 7, SiO formation is more efficient when Si is in neutral form. Thus, the self-shielding of Si in model @ activates a direct and efficient formation route of SiO by $\text{Si} + \text{OH} \rightarrow \text{SiO} + \text{H}$. On the contrary, in models with lower mass-loss rate, SiO synthesis proceeds via the much less efficient Si^+ route.

The H₂O abundance is found to be low, reaching 10⁻⁶ for the highest mass-loss rate. As for OH, the H₂O wavelength dissociation threshold is longer than the ionization threshold of C, S, Si and even Fe or Mg. H₂O is not efficiently shielded by the gas and its increase with mass-loss rate is mostly due to the increase of the H₂ abundance. At the highest mass-loss rates ($\dot{M}_w \geq 2 \times 10^{-6} M_\odot \text{ yr}^{-1}$), H₂O is also destroyed though the reverse reaction H₂O + H → OH + H₂.

4.3. Results: dust-poor winds

The inclusion of a non-vanishing fraction of dust activates H₂ formation on dust (see Section 3), and introduces a new source of opacity for the radiation field. Figure 10 summarizes the influence of dust fraction Q/Q_{ref} on the asymptotic molecular abundances for the full set of wind models.

The inclusion of a small fraction of dust $Q/Q_{\text{ref}} = 10^{-3}$ increases H₂ abundances by a factor ~ 2 (Fig. 10-a). Over the explored range of wind mass-loss rates, this specific dust fraction is indeed close to the critical value above which H₂ formation on grains takes over gas phase formation (see Sec. 3). The chemistry of H₂ is consequently weakly affected. Similarly, the CO abundance is also weakly affected. This is because the opacity of the gas below $\lambda \leq 1100 \text{ \AA}$ is still dominated by carbon over most of wind models. Consequently, dust does not affect CO photodissociation rates and the CO abundance changes only by a factor ≈ 3 . On the contrary, this small amount of dust has a strong impact on the abundance of SiO and H₂O. Attenuation of the radiation field by this small amount of dust above $\lambda \geq 1100 \text{ \AA}$ shields SiO and H₂O, decreasing photodissociation rates. The attenuation by dust also triggers self-shielding of atomic species for lower-mass-loss rate ($\dot{M}_w = 10^{-6} M_\odot \text{ yr}^{-1}$), leading to an even stronger attenuation of the radiation field at long-wavelengths. Furthermore, regarding SiO, the Si⁺/Si transition activates the very efficient SiO formation route through Si. As a consequence, the critical mass-loss rate \dot{M}_w above which the wind is rich in SiO is lowered.

For larger Q/Q_{ref} ratios, formation of H₂ on dust takes over from gas-phase formation. Enhanced abundances of H₂ increase the formation rate of molecules whereas attenuation of the radiation field by dust reduces destruction rates. Figure 10 shows that CO, SiO, H₂O abundances increase by several orders of magnitude with increasing Q/Q_{ref} above the critical value $Q/Q_{\text{ref}} = 10^{-3}$. The overall impact of dust on CO and SiO content is to lower the critical mass-loss rate below which the gas is rich in CO and SiO. For example, whereas dust-free wind models are rich in CO for $\dot{M}_w \geq 5 \times 10^{-7} M_\odot \text{ yr}^{-1}$ and rich in SiO for $\dot{M}_w \geq 2 \times 10^{-6} M_\odot \text{ yr}^{-1}$, dusty-wind models with $Q/Q_{\text{ref}} = 10^{-2}$ are rich in CO for $\dot{M}_w \geq 10^{-7} M_\odot \text{ yr}^{-1}$ and rich in SiO for $\dot{M}_w \geq 5 \times 10^{-7} M_\odot \text{ yr}^{-1}$. Interestingly, above those critical mass-loss rates, CO and SiO constitute the main carbon and silicon carriers.

In contrast, the H₂O abundance has a more complex dependency on Q/Q_{ref} and \dot{M}_w . H₂O reaches large abundances only for at high mass-loss rates and for rather large fraction of dust ($Q/Q_{\text{ref}} \geq 10^{-2}$). When the wind is sufficiently shielded by dust, destruction via the reverse reaction H₂O + H → H₂ + OH limits the abundance of H₂O. Being rich in atomic hydrogen, dust-free and dust-poor winds are hostile to the formation and survival of H₂O.

4.4. Time dependent chemistry

For all models, chemistry is found to be out-of-equilibrium, leading to asymptotic abundances that are somewhat smaller than steady-state abundances. As the density and the radiation field drop with z due to geometrical dilution and attenuation, the ratio between the chemical and the dynamical timescales increases as $V_j/(z n_{\text{H}}(z))$ for two-body reactions and as $V_j/(z F(z))$ for photoreactions, where $F(z)$ is the local FUV photon flux. The flow thus necessarily undergoes transitions beyond which part or all of the chemistry is "frozen". In the models presented here, we find that these transitions occurs around $z \approx z_0$. We note, however, that out-of-equilibrium effects do not explain the global trend with mass-loss rate (i.e. wind density) and with dust fraction, and only reduce the overall asymptotic abundances by a factor less than 4.

4.5. Summary

In this section, the chemistry of dust-free and dust-poor winds have been investigated by the use of parameterized wind models that include time-dependent chemistry and the attenuation of the radiation field. Our results for warm wind models ($T_{\text{K}} = 1000 \text{ K}$) are summarized in Fig. 10. The overall molecular content of wind models increases with mass-loss rate of the wind and with the dust fraction. Dust-free and dust-poor winds are atomic but the small fraction of H₂, formed essentially via H⁻ regulates the synthesis of other molecules. The survival of these molecules is insured by the attenuation of the radiation field by atomic species, and by dust, if any. The attenuation of the radiation field by atomic species proceeds through self-shielding, a process that depends critically on the column density of the absorbing species. It results in the presence of density or equivalently, mass-loss rate thresholds above which specific molecules are very abundant. Those thresholds depend on both the specific species and the dust fraction.

5. Discussion

Our results on disk wind chemistry have been obtained from a simple parametric wind model. The main advantage of this wind model is to be based on a simple geometry that allows a deep exploration of the parameter space and a detailed treatment of the radiative transfer. A number of limitations regarding the model presented here have to be taken into account before comparing our results to observations.

5.1. Attenuation in the wind

The radiative transfer is reduced to a 1D geometry by assuming that the radiation field is attenuated along the computed streamline. In a 2D geometry, the shielding of a streamline is provided by inner streamlines of the wind. This is especially true at the base of the wind, where photons coming from the accreting central object are impinging the streamline almost transversely. However, for most of the models presented here, the decline of the radiation field at the base of the wind $z < R_0$ is mostly caused by geometrical dilution, an effect that is properly taken into account by our 1D model. Species that contribute to the attenuation of the radiation field are mostly formed around $z \approx 25R_0$. At this distance, FUV photons propagate almost parallel to the streamlines and our 1D approximation is valid.

Our model also computes the attenuation of the radiation field by a limited number of species. As shown in Section 4,

attenuation by atomic species is a key process for the survival of molecules. Because of their long-wavelength dissociation thresholds, molecules such as OH or H₂O can not be efficiently shielded by the considered atoms, namely C, Si, S, Mg, Fe. In this context, other elements that exhibit longer-wavelength dissociation thresholds such as Al, Ca, Li could shield important molecules. However, our models show that in the absence of dust the attenuation by Mg and Fe is negligible for $\dot{M}_w \leq 10^{-6} M_\odot \text{ yr}^{-1}$. Thus, rarer elements that have also similar photoionisation cross-sections and similar recombination rates are expected to have a negligible contribution to the opacity of the gas.

5.2. Thermal structure and shocks

In this exploratory study, we considered only isothermal laminar disk wind models. The computation of thermal-balance is beyond the scope of this paper. The isothermal assumption is motivated by detailed thermal balance calculations in self-similar MHD disk winds showing that ambipolar diffusion is a robust heating mechanism able to balance adiabatic and radiative cooling, and naturally leads to a rather flat temperature profile (Safier 1993; Garcia et al. 2001). Depending on the disk wind mass-loss rate, the asymptotic temperature for $R_0 \approx 0.2$ au varies from 500 K to 4000 K (Panoglou et al. 2012; Yvart et al. 2016), in line with our assumed fiducial temperature of 1000 K. Similar calculations for a non-self-similar "X-wind" from the inner disk edge (Shang et al. 2002) also show a quasi-isothermal behavior on inner streamlines; hence it appears to be a generic property of MHD disk winds that undergo large-scale collimation. In contrast, models of stellar winds heated by ambipolar diffusion exhibited a decline of temperature at large distance (Ruden et al. 1990), due to the lack of magnetic collimation and the much smaller acceleration scale of a few R_\star (see discussion in Section 4.4.3 of Garcia et al. 2001). Note that the shielding of the wind is not expected to be sensitive to the thermal structure of the jet, since it relies on electron recombination and charge exchange rate coefficients that do not strongly depend on the temperature. The local radiation field computed in this work thus remains valid for warmer or cooler winds. On the other hand, it should be kept in mind that asymptotic molecular abundances would be significantly lower at wind temperatures below 1000 K (see Fig. 6-a).

In reality, shocks are likely to also contribute to the heating and compression of the gas, and impact molecule synthesis. Millimeter and sub-millimeter interferometric observations of Class 0 molecular jets show that high velocity components of molecular lines are spatially resolved as a series of knotty structures. Detection of proper motions of these knots (Lee et al. 2015), as well as detailed kinematical properties (Santiago-García et al. 2009; Tafalla et al. 2017) suggest that they are tracing internal shocks produced by time-variability in ejection velocity (Raga et al. 1990; Stone & Norman 1993). Numerical simulations including dust-free chemistry of H₂, but neglecting UV radiation field, shows that the H₂ abundance is indeed increased due to the increase of density in the post-shock gas (Raga et al. 2005).

The effect of time-variability in the flow is not included in our simplified laminar wind model. However, our results allow us to investigate qualitatively the possible impact of internal shocks on molecule formation. In Sections 3 and 4, we show that high molecular abundances are reached in dust-free or dust-poor winds if it is warm with temperatures between ≈ 800 and ≈ 3000 K (see Fig. 6-a), dense (see Fig. 6-b), and well shielded by the gas (see Fig. 9). The impact of shocks is to increase locally

the temperature and the density from their initial values. Both effects drive up molecular abundances compared to a laminar wind with the same equilibrium temperature and average mass-flux. At larger distance, all the successive internal shocks located between the protostar and z would also increase the gas attenuation of the radiation field, increasing even more the molecular richness of the wind. However, on large scale, the interstellar radiation field or the radiation field generated locally by strong shocks (eg. Tappe et al. 2012) is expected to take over from the protostellar radiation field. Hence, asymptotic chemical abundances presented in Fig. 10, neglecting the effect of shocks, should be considered as lower limits if the wind equilibrium temperature is $T_K \geq 800$ K, and if the protostellar radiation field dominates over other sources of FUV field. Otherwise, the peak abundances reached behind shocks could be lower than in Fig. 10 if molecule formation in the shocked gas is slower than the timescale to cool below ≈ 800 K.

Therefore, the precise quantitative impact of shocks remains to be constrained by detailed shock modeling, including self-consistent thermal balance. However, the overall decrease of molecular abundances with the decline of mass-loss rate and dust fraction remains a robust prediction of our model.

5.3. Observational perspective

5.3.1. Mass-loss rates

Clarifying the contribution of high velocity jets to mass and energy extraction during protostar formation remains an important observational challenge. Mass, momentum, and energy fluxes of deeply embedded Class 0 jets are usually derived from spectrally and spatially resolved CO rotational lines assuming a standard reference CO abundance of $x(\text{CO}) = x_{\text{ref}} \approx 10^{-4}$ (eg. Podio et al. 2016). Therefore, the observable quantity is not the true wind mass flux \dot{M}_w but the "observed" mass-flux \dot{M}_{obs} derived from CO observations assuming a standard CO abundance, namely

$$\dot{M}_{\text{obs}} = \frac{x(\text{CO})}{10^{-4}} \dot{M}_w. \quad (21)$$

Our models show that if the jet is dust-free or dust-poor, this assumption on the CO abundance may lead to large errors on the derived energetic properties of jets. Indeed, the mass-flux will be overestimated by a factor ~ 3.6 when all of elemental carbon is in the form of CO (i.e. for the highest \dot{M}_w or $Q/Q_{\text{ref}} \approx 0.1$), but underestimated by orders of magnitude at lower \dot{M}_w or lower Q/Q_{ref} . Interestingly, we find that when the CO abundance is $x(\text{CO}) \geq 10^{-6}$, neutral carbon and CO are the main carbon carriers (see Fig. 10). It suggests that sub-millimeter CI lines could be used together with CO to constrain the true CO abundance vs H and measure the true mass-flux of the jet.

Alternatively, our models suggest that ratios of molecular abundances could be used in conjunction with the observed \dot{M}_{obs} to estimate the dust content of the wind and its true mass-flux. This is shown in the next section.

5.3.2. Dust content

Our model results have shown that for a given wind temperature T_K , the molecular content is very sensitive to the precise dust fraction, suggesting that chemistry could be used as a unique tool to constrain the presence of dust in protostellar jets, and by way of consequence constrain their launching radius. Here we illustrate this point using our grid our laminar, isothermal disk

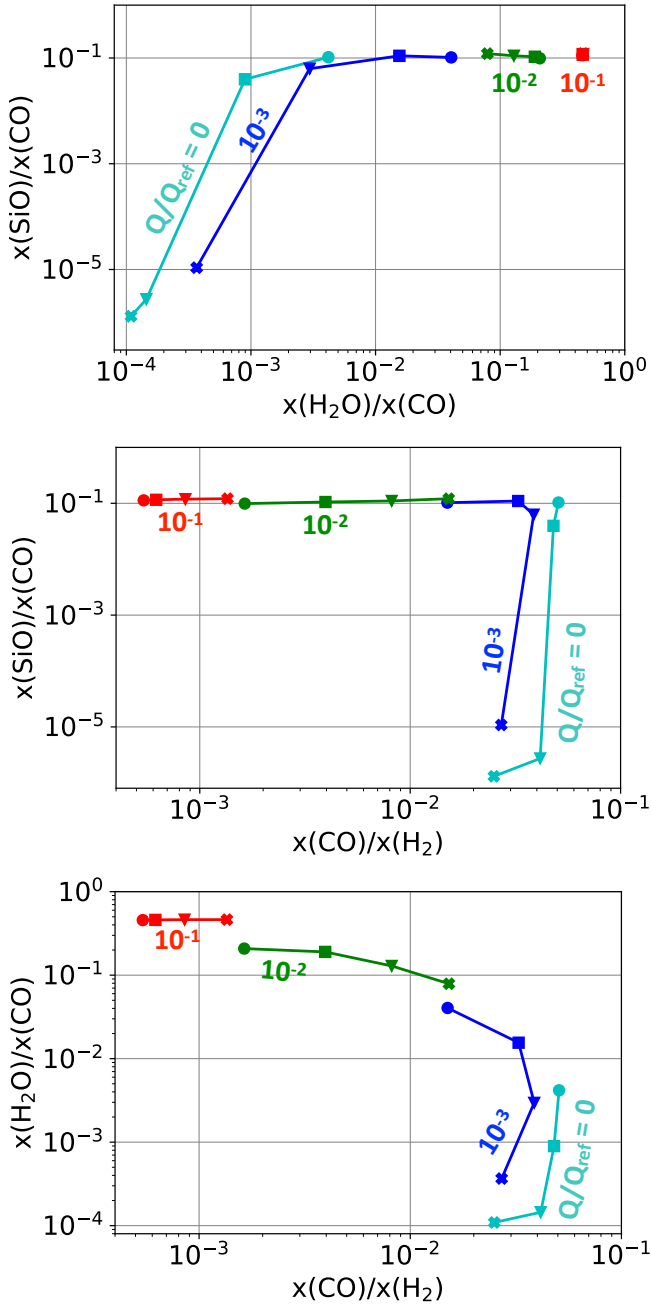


Fig. 11. Asymptotic abundance ratios for a streamline launched at $R_0 = 0.15$ au in the disk, for dust-free models (cyan) and dust-poor models with $Q/Q_{\text{ref}} = 10^{-3}$ (blue), 10^{-2} (green) and 0.1 (red) and for different values of $\dot{M}_w = 5 \times 10^{-7}$ (crosses), 10^{-6} (triangles), 2×10^{-6} (squares), and 5×10^{-6} (circles) $M_\odot \text{ yr}^{-1}$. All other parameters are kept constant to the values given in the footnote of Table 3. Note that the variations of the ratios with \dot{M}_w is due to the variations of n_{H}^0 , n_{H}^0/G_0^0 , and n_{H}^0/W^0 with \dot{M}_w , as indicated in eqs. 19, 17, and 16.

wind models with a temperature of $T_K = 1000$ K, recalling that our exact results depend on specific choices of fixed parameters given in the footnote of Table 3.

We first display in Fig. 11 the correlation between abundance ratios among brightest molecular jet tracers, namely CO/H₂, SiO/CO, H₂O/CO, obtained for $0 \leq Q/Q_{\text{ref}} \leq 10^{-1}$ and $5 \times 10^{-7} \leq \dot{M}_w \leq 5 \times 10^{-6}$, i.e. for objects with high mass loss rates. For all dust poor models, the $x(\text{CO})/x(\text{H}_2)$ ratio is found to be larger than 5×10^{-4} , in contrast with the standard ratio of

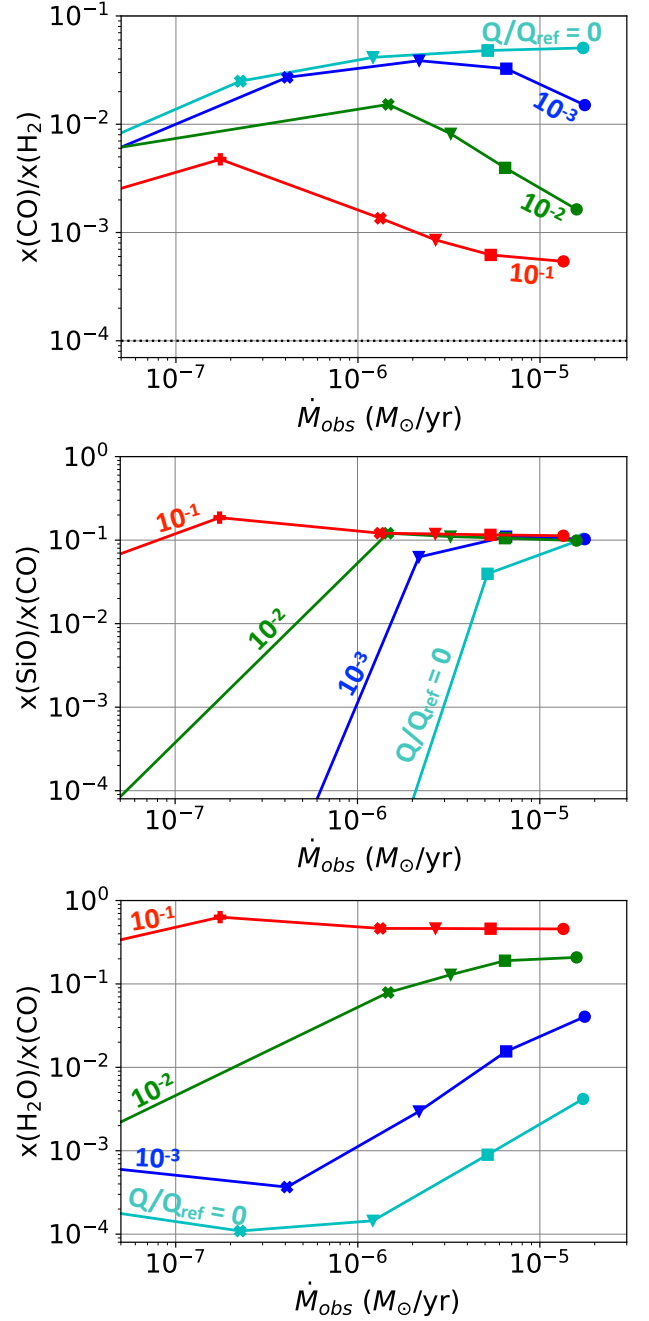


Fig. 12. Asymptotic abundance ratios for a streamline launched at $R_0 = 0.15$ au in the disk as function of the "observed" mass-flux \dot{M}_{obs} (see eq. 21), for dust-free models (cyan) and dust-poor models with $Q/Q_{\text{ref}} = 10^{-3}$ (blue), 10^{-2} (green) and 0.1 (red) and for different values of $\dot{M}_w = 10^{-7}$ (straight crosses), 5×10^{-7} (crosses), 10^{-6} (triangles), 2×10^{-6} (squares), and 5×10^{-6} (circles) $M_\odot \text{ yr}^{-1}$. All other parameters are kept constant to the values given in the footnote of Table 3. In particular $T_K = 1000$ K.

$\approx 10^{-4}$ derived in dusty molecular environments. Such a high ratio would thus directly point toward a small dust fraction $\ll 1$. However, it may also be seen that all our models follow almost the same well-defined "path" in these ratio-ratio plots; in other words, there is a strong degeneracy between \dot{M}_w (in effect n_{H}^0) and Q/Q_{ref} in the sense that the same ratio-ratio pair may be obtained by increasing one parameter and decreasing the other. Such plots are therefore not able by themselves to determine the dust fraction Q/Q_{ref} and true mass-flux precisely. However, they

do provide a good validation test of the underlying hypotheses in our simple laminar wind models, as all observations should lie close to the predicted curves.

In Fig. 12, we present a more powerful observational diagnostic of the dust fraction, where the same ratios are plotted as a function of the "observable" (two-sided) mass-flux \dot{M}_{obs} (see eq. 21). The plots start at $\dot{M}_{\text{obs}} = 10^{-7} M_{\odot}/\text{yr}$, which is the minimum detectable mass-flux in CO assuming a threshold beam-averaged column density of $N_{\text{CO}} = 3 \times 10^{15} \text{ cm}^{-2}$, a beam size of $3 \times 10^{14} \text{ cm} = 20 \text{ au}$, and a jet speed of 100 km s^{-1} . It may be seen that the degeneracy between density and dust fraction is lifted, in different ways for the different ratios.

The curve of $x(\text{CO})/x(\text{H}_2)$ vs \dot{M}_{obs} is found to provide a good diagnostic of the dust fraction, except for small \dot{M}_{obs} near the detection limit or for very dust-poor winds with $Q/Q_{\text{ref}} \leq 10^{-3}$ where curves come too close to discriminate. Measuring $N(\text{CO})/N(\text{H}_2)$ in protostellar jets is challenging since pure rotational and ro-vibrational lines of H_2 , and sub-millimeter lines of CO have very different upper energy levels and so are not necessarily tracing the same region of the jet. Probing simultaneously pure rotational lines of H_2 and high-J lines of CO would help to circumvent this problem. In that perspective, future JWST observations, in synergy with *Herschel* data would help to probe the dust content of high velocity jets.

In contrast to CO/H_2 , the SiO/CO ratio is very sensitive to the dust fraction even for small \dot{M}_{obs} and small Q/Q_{ref} . SiO is routinely observed though its submillimeter rotational transitions along with low-lying rotational transitions of CO (Bachiller et al. 1991; Guilloteau et al. 1992; Tychoniec et al. 2019). These lines having similar upper energy levels, they can be used to derive abundance ratio, though opacity effects can complicate the analysis (Cabrit et al. 2012). Because of the increase of n_{H}^0 with \dot{M}_{w} (see Eq. 19), our 1D laminar wind model predicted that SiO will reach its maximum abundance only above a critical mass-loss rate that depends on the precise dust fraction (Fig. 10). Figure 12 shows that even though the rise of SiO/CO with \dot{M}_{obs} is not as steep as $x(\text{SiO})$ versus \dot{M}_{w} in Figure 10, it would be possible to constrain the dust fraction from these curves if $\text{SiO}/\text{CO} < 0.1$. However, when the maximum possible amount of gas-phase SiO is reached for a given dust fraction, the SiO/CO abundance ratio is found to be remarkably constant with a value of about 0.1. In that case, the observed \dot{M}_{obs} only sets a lower limit to the dust fraction. In HH212, Cabrit et al. (2012) estimated a ratio $\text{SiO}/\text{CO} > 0.04$ while Lee et al. (2007) estimated $\dot{M}_{\text{obs}} \approx 2 \times 10^{-6} M_{\odot}/\text{yr}$. This suggests a lower limit $Q/Q_{\text{ref}} \geq 10^{-3}$. Joint observations of the SiO/CO and CO/H_2 abundance ratios together with \dot{M}_{obs} could be used to derive the combination of mass-loss rate and dust fraction in protostellar jets.

We recall that if SiO is formed in shocks and if the wind equilibrium temperature is $T_{\text{K}} \geq 800 \text{ K}$, the above diagnostic curves for laminar wind models will overestimate the true dust fraction. Since SiO is shielded by S and Si, we also expect to find a correlation between high column density of atomic sulfur and silicon, and high abundances of SiO. In that perspective, observations of the [SI] line at $25.2 \mu\text{m}$ by JWST in synergy with ALMA will be of interest.

The ratio $\text{H}_2\text{O}/\text{CO}$ vs \dot{M}_{obs} appears to be another good diagnostic for the dust content of the jets. Figure 11 shows that the $\text{H}_2\text{O}/\text{CO}$ abundance ratio depends on both the mass-loss rate and the dust fraction, and we predict rather low H_2O abundances in dust-poor jets. On-source water spectra have been acquired towards a large sample of low-mass protostars in the course of the WISH and WILL Key Programs (van Dishoeck et al. 2011; Mottram et al. 2017). HIFI observation have unveiled

high-velocity bullets towards 4 out of 29 Class 0 sources of the WISH sample (Kristensen et al. 2012). The $\text{H}_2\text{O}/\text{CO}$ abundance ratio is estimated to be $\approx 1 - 10^{-1}$ for mass-loss rates of about $\dot{M}_{\text{obs}} \approx 10^{-5} M_{\odot} \text{ yr}^{-1}$ (Kristensen et al. 2011; Hirano et al. 2010). Figure 12 shows that this is in line with our laminar wind models with $Q/Q_{\text{ref}} \geq 3 \times 10^{-3}$.

Finally, since dust-poor winds are shielded by S and Si below $\lambda = 1500 \text{ \AA}$, we predict that H_2O is photodissociated by longer-wavelength photons. Interestingly, it corresponds to the photodissociation of water through the A state that produces OH in vibrationally hot but rotationally cold state (van Harrevelt & van Hemert 2001). Thus, in the absence on an extra source of UV photons, OH would be expected to produce little mid-IR line from rotationally excited levels but strong ro-vibrational lines in the near-IR. This prediction can also be tested by future JWST MIRI and NIRSPEC observations. Again, shock models should be developed to properly derive the dust content in these molecular bullets. Comparison with other oxygen bearing species such as OH or atomic oxygen would also allow to better constrain dust-poor models.

5.4. Comparison with stellar wind models

Our work demonstrates that disk winds launched within the silicate dust sublimation radius should be poor in H_2 , with correspondingly high ratios of CO/H_2 . This unique feature of dust-poor chemistry was already identified in the context of stellar winds by previous authors (Rawlings et al. 1988; Glassgold et al. 1989; Ruden et al. 1990; Glassgold et al. 1991). With the exception of Ruden et al. (who had H_2 formation dominated by H_2^+ in their network) most of them also found that photodetachment of H^- is limiting the gas-phase formation rate of H_2 . However, our dust-free disk wind models predict H_2 abundances that are two orders of magnitude larger than those in dust-free stellar wind models with a similar mass-loss rate. For example, our Class 0 model (a) predicts an asymptotic H_2 abundance of $\approx 5 \times 10^{-3}$ whereas the Case 1 model of Glassgold et al. (1991) predicts only $\approx 2 \times 10^{-5}$. This difference is ultimately due to the geometry of the wind. For equal mass-loss rate and constant $V_{\text{w}} \approx 100 \text{ km s}^{-1}$, the initial n_{H}/W ratio in our disk wind model is similar to isotropic stellar winds ($\approx 10^{13} \text{ cm}^{-3}$ for $\dot{M}_{\text{w}} \approx 2-3 \times 10^{-6} M_{\odot}/\text{yr}$; see Case 1 in Glassgold et al. 1991). However, the asymptotic n_{H}/W ratio in the disk wind is increased by a large factor $(z_0/r_0)^2$ whereas it remains constant in the stellar winds. This allows H^- to survive and form H_2 in larger abundances. On the other hand, a dust-free stellar wind that accelerates from the sonic point can reach an H_2 abundance closer to our model, as density at the wind base is higher for the same mass flux, leading to more efficient H_2 synthesis (see Case 2 of Glassgold et al. 1991).

Regarding the formation and survival of OH, CO, SiO and H_2O , most of the previous studies on dust-free stellar winds have discarded the impact of a UV excess, which turns to be of key importance in low-mass protostars with an accretion shock. A notable exception is Glassgold et al. (1991), who have shown that the inclusion of a strong FUV excess lead to a dramatic decrease of the abundances of H_2O , OH, SiO, whereas the abundance of CO was weakly affected. Our modeling explored for the first time a level of FUV excess adjusted self-consistently to the wind mass-flux, assuming a canonical ratio of \dot{M}_{w} to M_{acc} of 0.1. It shows that dust-free disk winds remain very rich in molecules above $\dot{M}_{\text{w}} \approx 10^{-6} M_{\odot} \text{ yr}^{-1}$ (for our adopted values of $T_{\text{K}}, R_{\text{in}}, R_{\text{out}}, V_{\text{j}}, R_{\text{*}}$, etc). Even though an effect of the temperature is not excluded, our disk wind model also exhibits higher n_{H}/G_0 ratio

and higher total column densities (for similar \dot{M}_w) than stellar wind models, causing more efficient self-shielding by S and Si and favoring the survival of molecular species against FUV photodissociation.

6. Conclusion

In this work, the chemistry and resulting molecular composition of disk winds launched within the dust sublimation radius has been explored by the use of single point and stationary wind models. Our results show that formation of H_2 through H^- (electron catalysis) is a viable and dominant pathway to produce H_2 in dust-free disk winds. However, this route is not efficient enough to convert all atomic hydrogen into H_2 . It results that dust-free winds are atomic, in line with stellar wind models (Glassgold et al. 1991). The inclusion of surviving dust has a significant chemical impact on H_2 for $Q/Q_{\text{ref}} \geq 10^{-3}$, where $Q_{\text{ref}} \equiv 6 \times 10^{-3}$ is a reference dust-to-gas mass ratio. Above this value, the H_2 abundance in dust-poor winds depends on the dust fraction.

Our results also demonstrate that despite the low abundance of H_2 , dust-free and dust-poor disk winds can be rich in molecules such as CO, SiO or H_2O . Molecular richness of dust-free winds depends critically on the properties of the wind. High temperatures ($T_K > 800$ K) are required to activate efficient and direct formation routes of these molecules through OH. The overall molecular content of wind models increases with mass-loss rate of the wind and with the dust fraction. The survival of these molecules is insured by the attenuation of the radiation field by atomic species, and by dust, if any. The attenuation of the radiation field by atomic species proceeds through continuum self-shielding, a process that critically depends on the column density of the absorbing species. It results in the presence of density or equivalently, mass-loss rate thresholds above which specific molecules are very abundant. Those thresholds depend both on the specific species, and on the dust fraction. The order in which molecules are abundant as the density and/or the dust fraction increases is CO, SiO and H_2O . CO is abundant when continuum self-shielding of atomic carbon is triggered whereas SiO and H_2O are abundant when self-shielding of S and Si is activated.

Our results allow to propose observational diagnostics to probe the presence of dust in warm molecular jets ($T_K \geq 800$ K). As already suggested by Glassgold et al. (1991) in the context of stellar winds, a CO/ H_2 abundance ratio larger than standard ISM value of 10^{-4} would be the primary evidence of dust-poor winds. The SiO abundance appears to be a promising diagnostic to estimate the precise dust fraction in the wind: the SiO/CO abundance ratio exhibits a step increase from a critical \dot{M}_w value that depends on the dust fraction. The H_2O /CO abundance ratio is also very sensitive to the dust fraction and to the density of the wind and could be used in combination with other oxygen bearing species.

The main limitation of our predictions resides in the assumption of a laminar and isothermal flow at $T_K = 1000$ K. Indeed, observations at high angular resolution show that molecules are present in shocks. Our models, together with Raga et al. (2005), suggest that internal shocks can locally enhance molecular abundances by increasing the temperature and the density of the gas. In the next paper of this series, shock models including the thermal balance will be investigated. Synthetic predictions of line intensities will allow to identify the most promising atomic and molecular transitions to constrain the presence of dust in jets. In that perspective, the present modeling constitutes a necessary step toward shock modeling by computing preshock con-

ditions (chemical abundances and local UV field) from which shock models can be run.

Our work shows that chemistry is a powerful tool to unravel the dust content of protostellar jets. Future JWST observations, in combination with ALMA and *Herschel* data will be able to provide key information on the launching region of the jets. If jets are dust-free or dust-poor, the chemical inventory of jets will give access to elemental abundances of the inner regions of protostellar disks and uncover key physical processes at stake during this early phase of star formation.

Acknowledgements. This work is part of the research programme Dutch Astrochemistry Network II with project number 614.001.751, which is (partly) financed by the Dutch Research Council (NWO). This work was also supported by the French program Physique et Chimie du Milieu Interstellaire (PCMI) funded by the Conseil National de la Recherche Scientifique (CNRS) and Centre National d'Etudes Spatiales (CNES).

References

- Anderson, J. M., Li, Z.-Y., Krasnopolsky, R., & Blandford, R. D. 2003, *ApJ*, 590, L107
- Armitage, P. J. 2011, *ARA&A*, 49, 195
- Asplund, M., Grevesse, N., Sauval, A. J., & Scott, P. 2009, *ARA&A*, 47, 481
- Bachiller, R., Martin-Pintado, J., & Fuente, A. 1991, *A&A*, 243, L21
- Barinova, G. & van Hemert, M. C. 2006, *ApJ*, 636, 923
- Bergin, E., Calvet, N., D'Alessio, P., & Herczeg, G. J. 2003, *ApJ*, 591, L159
- Black, J. H. & van Dishoeck, E. F. 1987, *ApJ*, 322, 412
- Cabrit, S. 2002, in *EAS Publications Series*, Vol. 3, *EAS Publications Series*, ed. J. Bouvier & J.-P. Zahn, 147–182
- Cabrit, S. 2007a, *Jets from Young Stars: The Need for MHD Collimation and Acceleration Processes*, ed. J. Ferreira, C. Dougados, & E. Whelan, Vol. 723, 21
- Cabrit, S. 2007b, in *IAU Symposium*, Vol. 243, *Star-Disk Interaction in Young Stars*, ed. J. Bouvier & I. Appenzeller, 203–214
- Cabrit, S., Codella, C., Gueth, F., & Gusdorf, A. 2012, *A&A*, 548, L2
- Cabrit, S., Codella, C., Gueth, F., et al. 2007, *A&A*, 468, L29
- Canto, J. & Raga, A. C. 1991, *ApJ*, 372, 646
- Cizek, M., Horáček, J., & Domcke, W. 1998, *Journal of Physics B Atomic Molecular Physics*, 31, 2571
- Coppola, C. M., Longo, S., Capitelli, M., Palla, F., & Galli, D. 2011, *ApJS*, 193, 7
- De Colle, F., Cerqueira, A. H., & Riera, A. 2016, *ApJ*, 832, 152
- Draine, B. T. 1978, *ApJS*, 36, 595
- Draine, B. T. & Lee, H. M. 1984, *ApJ*, 285, 89
- Federman, S. R., Glassgold, A. E., & Kwan, J. 1979, *ApJ*, 227, 466
- Fendt, C. 2011, *ApJ*, 737, 43
- Ferreira, J., Dougados, C., & Cabrit, S. 2006, *A&A*, 453, 785
- Flower, D. R., Le Bourlot, J., Pineau des Forêts, G., & Cabrit, S. 2003, *MNRAS*, 341, 70
- Flower, D. R. & Pineau des Forêts, G. 2003, *MNRAS*, 343, 390
- Flower, D. R. & Pineau des Forêts, G. 2013, *MNRAS*, 436, 2143
- Flower, D. R. & Pineau des Forêts, G. 2015, *A&A*, 578, A63
- Forrey, R. C. 2013, *ApJ*, 773, L25
- Galli, D. & Palla, F. 1998, *A&A*, 335, 403
- Galli, D. & Palla, F. 2013, *ARA&A*, 51, 163
- Garcia, P. J. V., Ferreira, J., Cabrit, S., & Binette, L. 2001, *A&A*, 377, 589
- Glassgold, A. E., Mamon, G. A., & Huggins, P. J. 1989, *ApJ*, 336, L29
- Glassgold, A. E., Mamon, G. A., & Huggins, P. J. 1991, *ApJ*, 373, 254
- Godard, B., Pineau des Forêts, G., Lesaffre, P., et al. 2019, *A&A*, 622, A100
- Greaves, J. S. & Rice, W. K. M. 2010, *MNRAS*, 407, 1981
- Guilloteau, S., Bachiller, R., Fuente, A., & Lucas, R. 1992, *A&A*, 265, L49
- Harsono, D., Bjerkerli, P., van der Wiel, M. H. D., et al. 2018, *Nature Astronomy*, 2, 646
- Heays, A. N., Bosman, A. D., & van Dishoeck, E. F. 2017, *A&A*, 602, A105
- Hirano, N., Ho, P. T. P., Liu, S.-Y., et al. 2010, *ApJ*, 717, 58
- Hollenbach, D. & McKee, C. F. 1979, *ApJS*, 41, 555
- Kristensen, L. E., van Dishoeck, E. F., Bergin, E. A., et al. 2012, *A&A*, 542, A8
- Kristensen, L. E., van Dishoeck, E. F., Tafalla, M., et al. 2011, *A&A*, 531, L1
- Kurosawa, R., Harries, T. J., & Symington, N. H. 2006, *MNRAS*, 370, 580
- Laor, A. & Draine, B. T. 1993, *ApJ*, 402, 441
- Le Petit, F., Nehmé, C., Le Bourlot, J., & Roueff, E. 2006, *ApJS*, 164, 506
- Lee, C.-F., Hirano, N., Zhang, Q., et al. 2015, *ApJ*, 805, 186
- Lee, C.-F., Ho, P. T. P., Hirano, N., et al. 2007, *ApJ*, 659, 499
- Lee, C.-F., Ho, P. T. P., Li, Z.-Y., et al. 2017, *Nature Astronomy*, 1, 0152

Lee, H. H., Herbst, E., Pineau des Forets, G., Roueff, E., & Le Bourlot, J. 1996, A&A, 311, 690

Lenzuni, P., Gail, H.-P., & Henning, T. 1995, ApJ, 447, 848

Lesaffre, P., Pineau des Forêts, G., Godard, B., et al. 2013, A&A, 550, A106

Manara, C. F., Morbidelli, A., & Guillot, T. 2018, A&A, 618, L3

Mathis, J. S., Mezger, P. G., & Panagia, N. 1983, A&A, 500, 259

Mathis, J. S., Rimpl, W., & Nordsieck, K. H. 1977, ApJ, 217, 425

McClure, M. K. 2019, arXiv e-prints, arXiv:1910.06029

McClure, M. K. & Dominik, C. 2019, arXiv e-prints, arXiv:1910.07345

McLaughlin, B. M., Stancil, P. C., Sadeghpour, H. R., & Forrey, R. C. 2017, Journal of Physics B Atomic Molecular Physics, 50, 114001

Mottram, J. C., van Dishoeck, E. F., Kristensen, L. E., et al. 2017, A&A, 600, A99

Panoglou, D., Cabrit, S., Pineau Des Forêts, G., et al. 2012, A&A, 538, A2

Podio, L., Codella, C., Gueth, F., et al. 2016, A&A, 593, L4

Raga, A. & Cabrit, S. 1993, A&A, 278, 267

Raga, A. C., Canto, J., Binette, L., & Calvet, N. 1990, ApJ, 364, 601

Raga, A. C., Williams, D. A., & Lim, A. J. 2005, Rev. Mexicana Astron. Astrofis., 41, 137

Ramaker, D. E. & Peek, J. M. 1973, Atomic Data, 5, 167

Rawlings, J. M. C., Williams, D. A., & Canto, J. 1988, MNRAS, 230, 695

Röllig, M., Abel, N. P., Bell, T., et al. 2007, A&A, 467, 187

Ruden, S. P., Glassgold, A. E., & Shu, F. H. 1990, ApJ, 361, 546

Safier, P. N. 1993, ApJ, 408, 115

Santiago-García, J., Tafalla, M., Johnstone, D., & Bachiller, R. 2009, A&A, 495, 169

Shang, H., Glassgold, A. E., Shu, F. H., & Lizano, S. 2002, ApJ, 564, 853

Stancil, P. C., Babb, J. F., & Dalgarno, A. 1993, ApJ, 414, 672

Stancil, P. C., Kirby, K., Gu, J. P., et al. 2000, A&AS, 142, 107

Stone, J. M. & Norman, M. L. 1993, ApJ, 413, 210

Tabone, B., Cabrit, S., Bianchi, E., et al. 2017, A&A, 607, L6

Tabone, B., Raga, A., Cabrit, S., & Pineau des Forêts, G. 2018, A&A, 614, A119

Tafalla, M., Santiago-García, J., Hacar, A., & Bachiller, R. 2010, A&A, 522, A91

Tafalla, M., Su, Y. N., Shang, H., et al. 2017, A&A, 597, A119

Tappe, A., Forbrich, J., Martín, S., Yuan, Y., & Lada, C. J. 2012, ApJ, 751, 9

Tychoniec, Ł., Hull, C. L. H., Kristensen, L. E., et al. 2019, arXiv e-prints, arXiv:1910.07857

van Dishoeck, E. F., Kristensen, L. E., Benz, A. O., et al. 2011, PASP, 123, 138

van Harrevelt, R. & van Hemert, M. C. 2001, J. Chem. Phys., 114, 9453

Visser, R., Geers, V. C., Dullemond, C. P., et al. 2007, A&A, 466, 229

Visser, R., van Dishoeck, E. F., & Black, J. H. 2009, A&A, 503, 323

White, M. C., Bicknell, G. V., Sutherland, R. S., Salmeron, R., & McGregor, P. J. 2016, MNRAS, 455, 2042

Yvart, W., Cabrit, S., Pineau des Forêts, G., & Ferreira, J. 2016, A&A, 585, A74

Zinnecker, H., Bastien, P., Arcoragi, J.-P., & Yorke, H. W. 1992, A&A, 265, 726

Appendix A: Radiation field

Throughout this work, we model the radiation field by means of two components.

- A FUV component equal to the FUV part of the standard interstellar radiation field (ISRF, Mathis et al. 1983) and rescaled by the parameter G_0 . Following the fitting formula adopted in the Meudon PDR code⁵ (Le Petit et al. 2006), the FUV part is modelled by a mean specific intensity of

$$J_v^{FUV} = G_0 \times 107.2 \left(\tanh(4.07 \cdot 10^{-3} \lambda - 4.6) + 1 \right) \lambda^{-2.89}, \quad (\text{A.1})$$

with the wavelength λ in Å and $J_v^{ISRF,FUV}$ in $\text{erg s}^{-1} \text{cm}^{-2} \text{Å}^{-1}$. This formula fits the ISRF below $\lambda \approx 2000 \text{Å}$ (see Fig. A.1-b).

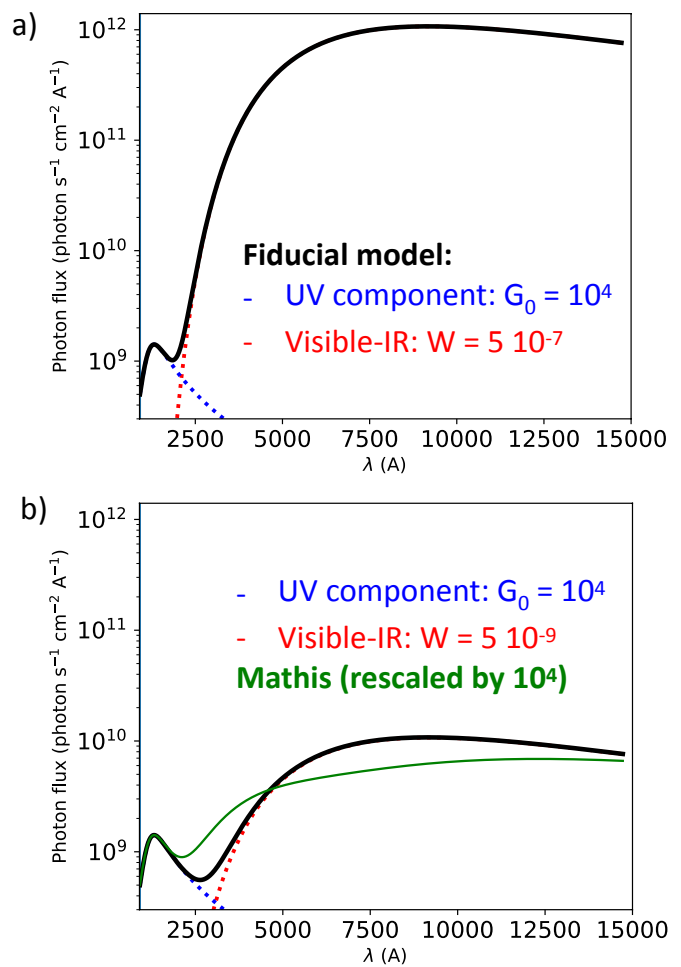


Fig. A.1. Mean intensity of the adopted radiation field for two sets of parameter $\{G_0, W\}$. The FUV and the visible components are in dotted blue and dotted red lines respectively and the total spectrum is in black solid line. a) Mean intensity of the radiation field adopted in Section 3 corresponding to $\{G_0 = 10^4, W = 5 \times 10^{-3}\}$. b) Mean intensity with the same FUV component but a weaker visible one ($\{G_0 = 10^4, W = 5 \times 10^{-9}\}$) overlaid on the Mathis ISRF scaled by $G_0 = 10^4$.

- A visible-NIR component modeled by a black-body emission at a temperature $T_{\text{vis}} = 4000 \text{ K}$, diluted by a factor W

$$J_v^{\text{visible}} = W \times B_v(T_{\text{vis}}). \quad (\text{A.2})$$

In section 3, W is used as a parametrization of the visible-NIR intensity. In section 4, this parameter is the dilution factor of the photospheric emission and can thus be written as

$$W(R) = \frac{1}{2} \left(1 - (1 - R_*^2/R^2)^{1/2} \right), \quad (\text{A.3})$$

where R_* is the stellar radius and R is the distance to the central object. For $R \gg R_*$ the dilution factor yields

$$W(R) = \frac{1}{4} \left(\frac{R_*}{R} \right)^2. \quad (\text{A.4})$$

Figure A.1-a shows the radiation fields adopted in Section 3. Figure A.1-b shows a radiation field $\{G_0 = 10^4, W = 5 \times 10^{-9}\}$ overlaid by the Mathis et al. (1983) ISRF scaled by $G_0 = 10^4$. The

⁵ see <https://ism.obspm.fr>

parametrized radiation field reproduces well the ISRF within a factor 2 from the visible ($\lambda \simeq 4000 \text{ \AA}$) to the NIR ($\lambda \simeq 15000 \text{ \AA}$). Thus, our parametrization gives also a good proxy for the shape of the ISRF for $W = 5 \times 10^{-13}$.

Appendix B: Updated chemical network

We review here chemical reactions and their adopted rate coefficients added to the chemical network of Godard et al. (2019). Reaction rate coefficients that are outdated or inaccurate in standard astrochemical databases (KIDA, UMIST, OSU) have been fitted from theoretical and experimental work in the form of a modified Arrhenius law.

Radiative association. Gas-phase formation routes of H_2 involving two-body reactions are initiated by radiative associations. As shown in Appendix C, the efficiency of these routes is directly proportional to the radiative association rate coefficient. It is thus crucial to get accurate rate coefficients, especially for the radiative association that is found to be dominant, namely between hydrogen and electron and between hydrogen and C^+ . Table B.1 compiles the radiative association rate coefficients adopted in this work together with references used to fit the rate coefficients. Original data and adopted fits are plotted in Fig. B.1.

Table B.1. Radiative association rate coefficients with hydrogen relevant for the formation of H_2 .

Reaction	Rate ($\text{cm}^3 \text{s}^{-1}$)	Ref.
$\text{e}^- + \text{H}$	$2.6 \times 10^{-16} \left(\frac{T_K}{300}\right)^{0.9}$	(1)
$\text{C}^+ + \text{H}$	$2.28 \times 10^{-17} \left(\frac{T_K}{300}\right)^{-0.42}$	(2)
$\text{Si}^+ + \text{H}$	$1.18 \times 10^{-17} \left(\frac{T_K}{300}\right)^{-0.12}$	(3)
$\text{S}^+ + \text{H}$	8.13×10^{-21}	(3)
$\text{H}^+ + \text{H}$	$6.3 \times 10^{-19} \left(\frac{T_K}{300}\right)^{1.68}$	(4,5)

References. (1) McLaughlin et al. (2017); (2) Barinovs & van Hemert (2006); (3) Stancil et al. (2000); (4) Ramaker & Peek (1973); (5) Stancil et al. (1993)

Other chemical reactions associated to H_2 . Other reactions related to H_2 formation and added to the original network are reported in Table B.2.

Table B.2. H_2 related chemical reactions added to Godard et al. (2019). Photodetachment rate of H^- is given for a 4000 K black-body radiation field diluted by a factor W .

Reaction	Rate ($\text{cm}^3 \text{s}^{-1}$)	Reference
$\text{H}^- + \text{H} \rightarrow \text{H}_2 + \text{e}^-$	$1.3(-9)$	KIDA
$\text{H}^- + h\nu \rightarrow \text{H} + \text{e}^-$	$6.0(+5)W\text{s}^{-1}$	(3)
$\text{H}^- + \text{H}^+ \rightarrow \text{H} + \text{H}$	$2.3(-7)(T_K/300 \text{ K})^{-0.5}$	KIDA
$\text{H}^- + \text{H}^+ \rightarrow \text{H}_2^+ + \text{e}^-$	$8.4(-9)(T_K/300 \text{ K})^{-0.35}$	(4)
$\text{H} + \text{H} + \text{H} \rightarrow \text{H}_2 + \text{H}$	$2.6 \times 10^{-32} \left(\frac{T_K}{300 \text{ K}}\right)^{-0.34}$	Fit from (5)

References. (1) Cížek et al. (1998); (2) Coppola et al. (2011); (3) Heays et al. (2017); (4) Galli & Palla (1998); (5) Forrey (2013).

Mg charge-exchange network. Chemical reactions controlling the ionization state of magnesium added to the original chemical network are reported in table B.3.

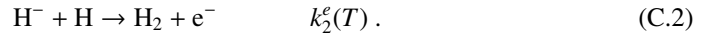
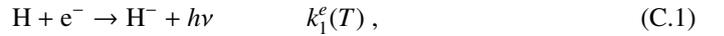
Appendix C: Analytical approach of H_2 formation in gas-phase

In this appendix we propose an analytic approach for the formation of H_2 in dust-free and dust-poor environments. Our goal is to derive analytical expression of boundaries defining the dominant formation route in the $\{n_{\text{H}}, W\}$ plane (see Fig. 3), and derive the analytical expression of the abundance of H_2 plotted in Fig. 4. To do so, formation rates of H_2 by H^- and by any XH^+ ion are first derived, taking into account photodestruction of these intermediates. Then, a comparison between various routes, including three-body reaction is given.

Appendix C.1: Formation rate by gas phase catalysis

Formation of H_2 through H^- and any ion XH^+ (with $\text{X}=\text{C}, \text{S}, \text{H} \dots$) is a two stage catalytic process. In this section, we derive the resulting formation rate of H_2 assuming steady state for the intermediate species H^- and XH^+ (Bodenstein approximation). Throughout this section, the gas is assumed to be neutral and atomic ($x(\text{H}) \simeq 1$), in line with our modeling results (Section 3, 4).

Electron catalysis. H_2 can be formed through the intermediate anion H^- , via a slow radiative attachment and a fast associative detachment:



The efficiency of this route depends on the survival of the intermediate H^- . In neutral medium, the main destruction route that can compete with the associative detachment (C.2) is the photodetachment of the fragile H^- anion by visible photons,



For a diluted black-body at 4000 K, H^- decays preferentially through the associative detachment (C.2) to produce H_2 if

$$n_{\text{H}}/W > n_{\text{H}}^{\text{crit}} \equiv \frac{k_{\phi}^{0,e}}{k_2^e} = 4.6 \times 10^{14} \text{ cm}^{-3}, \quad (\text{C.4})$$

where $k_{\phi}^{0,e}$ is the photodetachment rate by an undiluted black-body at 4000 K. Above this critical value, the efficiency of the electron catalysis is optimal. Defining

$$\eta \equiv \frac{n_{\text{H}}}{W n_{\text{H}}^{\text{crit}}}, \quad (\text{C.5})$$

a fraction

$$\frac{\eta}{1 + \eta} \quad (\text{C.6})$$

of the H^- formed by radiative association is converted in H_2 . The associative detachment or photodetachment being very fast, H^-

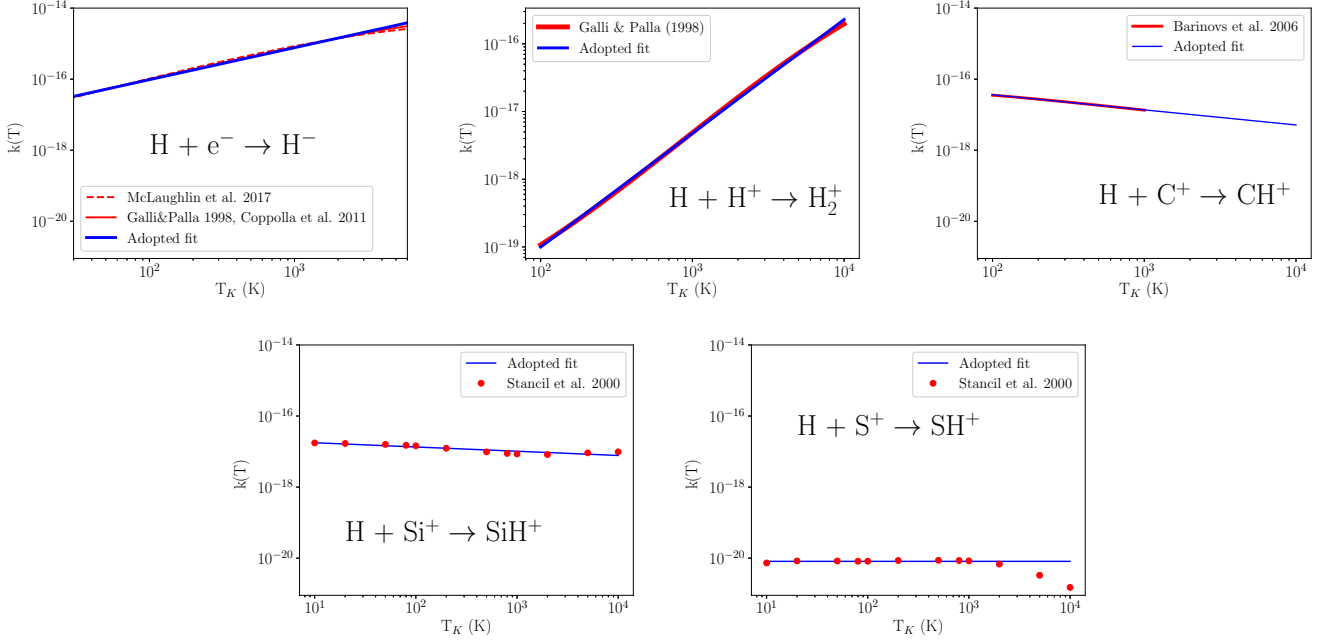


Fig. B.1. Adopted radiative association rate coefficients. Red lines and red dots are computed or measured rate coefficients taken from references indicated in Table B.1, and blue are the Arrhenius fits used in this work.

Table B.3. Magnesium chemical network added to Godard et al. (2019). All reaction but photoionization are from KIDA database.

Reaction	Rate ($\text{cm}^3 \text{s}^{-1}$)
$\text{Mg} + h\nu \rightarrow \text{Mg}^+ + e^-$	Cross-section from (1)
$\text{Mg}^+ + e^- \rightarrow \text{Mg} + h\nu$	$2.80 \times 10^{-12} (T_K/300K)^{-0.86}$
$\text{Mg} + \text{H}^+ \rightarrow \text{Mg}^+ + \text{H}$	1.1×10^{-9}
$\text{Mg} + \text{H}_3^+ \rightarrow \text{Mg}^+ + \text{H}_2 + \text{H}$	1×10^{-9}
$\text{Mg} + \text{C}^+ \rightarrow \text{Mg}^+ + \text{C}$	1.1×10^{-9}
$\text{Mg} + \text{HCO}^+ \rightarrow \text{Mg}^+ + \text{HCO}$	2.9×10^{-9}
$\text{Mg} + \text{H}_3\text{O}^+ \rightarrow \text{Mg}^+ + \text{H}_2\text{O} + \text{H}$	1×10^{-9}
$\text{Mg} + \text{H}_2\text{O}^+ \rightarrow \text{Mg}^+ + \text{H}_2\text{O}$	2.2×10^{-9}
$\text{Mg} + \text{O}_2^+ \rightarrow \text{Mg}^+ + \text{O}_2$	1.2×10^{-9}
$\text{Mg} + \text{NO}^+ \rightarrow \text{Mg}^+ + \text{NO}$	8.1×10^{-10}
$\text{Mg} + \text{S}^+ \rightarrow \text{Mg}^+ + \text{S}$	2.8×10^{-10}
$\text{Mg} + \text{SH}^+ \rightarrow \text{Mg}^+ + \text{SH}$	2.6×10^{-9}
$\text{Mg} + \text{SO}^+ \rightarrow \text{Mg}^+ + \text{SO}$	1×10^{-10}
$\text{Mg} + \text{H}_2\text{S}^+ \rightarrow \text{Mg}^+ + \text{H}_2\text{S}$	2.8×10^{-9}
$\text{Mg}^+ + \text{H} \rightarrow \text{Mg}^+ + \text{H}^+ + e^-$	$1.3 \times 10^{-13} (T_K/300K)^{-0.86} e^{-157890/T}$
$\text{Mg}^+ + \text{H}_2 \rightarrow \text{Mg}^+ + \text{H}_2^+ + e^-$	$1.1 \times 10^{-13} (T_K/300K)^{-0.86} e^{-179160/T}$
$\text{Mg}^+ + \text{H}_2 \rightarrow \text{Mg}^+ + \text{H} + \text{H} + e^-$	$3 \times 10^{-11} (T_K/300K)^{-0.86} e^{-52000/T}$
$\text{Mg}^+ + \text{He} \rightarrow \text{Mg}^+ + \text{He}^+ + e^-$	$1.1 \times 10^{-13} (T_K/300K)^{-0.86} e^{-285328/T}$

References. (1) Heays et al. (2017).

reaches steady-state abundances much faster than H_2 , in a typical equilibrium is: time scale of ⁶

$$t_{\text{H}^-} \simeq (k_1^e n_{\text{H}})^{-1} \simeq 8 \left(\frac{n_{\text{H}}}{10^8 \text{cm}^{-3}} \right)^{-1} \text{ s.} \quad (\text{C.7})$$

For $t \gg t_{\text{H}^-}$, the resulting H_2 formation rate of the full catalytic process, valid even when H_2 abundance is out-of-

⁶ At first order, stationary time scale of a chemical species corresponds to its destruction time scale.

equilibrium is:

$$R_{\text{elec}}^{\text{H}_2} = 3.4 \times 10^{-19} \left(\frac{x_e}{4.8 \cdot 10^{-4}} \right) \left(\frac{T_K}{1000K} \right)^{0.9} \frac{\eta}{1 + \eta} \left(\frac{n_{\text{H}}}{1 \text{cm}^{-3}} \right)^2 \text{ cm}^{-3} \text{ s}^{-1}. \quad (\text{C.8})$$

The efficiency of this route is directly proportional to the electron fraction. For $\eta \gg 1$, this rate does not depend on the rate of the fast associative attachment (C.2) but only on the rate of the

Table C.1. Formation rates of H_2 by electron and ionic catalysis in $cm^{-3} s^{-1}$. Rates for electron and ionic catalysis are parametrized according to equation (C.8) and (C.17) respectively. $n_H^{crit,X}$ is defined in equation (C.14). α is the H_2 formation rate in $cm^{-3} s^{-1}$ at $T_K = 1000$ K assuming a reference abundance of the catalyst of x_X . This reference value is the elemental abundance of the corresponding element for $X=C, S, Si$, and an abundance representative of dust-free wind for H^+ . The electron abundance corresponds to the one obtained if all atoms with an $IP < 13.6$ eV are ionized. Numbers in parentheses are powers of 10.

Catalyst	x_X	α ($cm^{-3} s^{-1}$)	β	$n_H^{crit,X}$ (cm^{-3})
e^-	4.8(-4)	3.35(-19)	0.9	.
C^+	3.55(-4)	4.88(-21)	-0.42	1.7
Si^+	3.35(-5)	3.42(-22)	-0.12	1.4
S^+	1.86(-5)	1.51(-25)	0	4.7
H^+	1.00(-6)	4.76(-24)	1.68	0.6

limiting slow radiative association (C.1), leading the a rate of

$$R_{elec}^{H_2} = 3.4 \times 10^{-19} \left(\frac{x_e}{4.8 \cdot 10^{-4}} \right) \left(\frac{T_K}{1000K} \right)^{0.9} \left(\frac{n_H}{1cm^{-3}} \right)^2 cm^{-3} s^{-1}. \quad (C.9)$$

If H_2 is predominantly formed through H^- and destroyed by photodissociation at a rate k_{photo} , the steady-state H_2 abundance is

$$x(H_2) = R_{elec}^{H_2} / (n_H k_{photo}). \quad (C.10)$$

For an unshielded Mathis radiation field rescaled by a factor G_0 , the steady-state H_2 abundance yields⁷

$$x(H_2) = 5.6 \times 10^{-9} \frac{x_e}{4.8 \cdot 10^{-4}} \left(\frac{T_K}{1000K} \right)^{0.9} \frac{n_H}{G_0} \frac{\eta}{1 + \eta}, \quad (C.11)$$

with η given in eq. (C.5).

Ionic catalysis. H_2 formation can also be catalyzed by any ion noted here X^+ , through the intermediate ion XH^+ . The process is made of a slow radiative association and a fast ion neutral reaction:



This route is the analogous of the former with ions being the catalyst. As for the latter, the efficiency of the catalytic process depends on the survival of XH^+ . In protostellar winds, the main destruction routes that can compete with reaction (C.13) are dissociative recombination that reduces the efficiency of the catalysis by a factor less than 30%, and by photodissociation. Unlike the fragile H^- , ionic intermediates XH^+ are photodestroyed by UV photons ($\lambda < 400$ nm). For an unshielded Mathis radiation field, reaction (C.13) dominates over photodissociation if

$$n_H / G_0 > n_H^{crit,X} \equiv \frac{k_\phi^{0,X}}{k_2^X}, \quad (C.14)$$

where $n_H^{crit,X}$ is given in Table C.1 for the main ions, and $k_\phi^{0,X}$ is the photodissociation rate of XH^+ by an unshielded Mathis radiation field. Below this critical value, photodissociation reduces the efficiency of the considered route. Defining

$$\eta_X \equiv \frac{n_H}{G_0 n_H^{crit,X}}, \quad (C.15)$$

a fraction

$$\eta_X \equiv \frac{n_H}{G_0 n_H^{crit,X}} \quad (C.16)$$

of the XH^+ formed by radiative association is converted in H_2 . As for H^- , XH^+ ions reach steady-state in very short time scales and yield to a total formation rate of H_2 by X^+ that can be written as

$$R_{X^+} = \alpha \left(\frac{x(X^+)}{x_X} \right) \left(\frac{T}{1000K} \right)^\beta \frac{\eta_X}{1 + \eta_X} \left(\frac{n_H}{1cm^{-3}} \right)^2, \quad (C.17)$$

where x_X is a reference value for the abundance $x(X^+)$ of the catalyst X^+ , and α, β are given in Table C.1.

Appendix C.2: Comparison between routes

Dust-free. Formation rates of H_2 by H^- and XH^+ deduced from parameters and reported in Table C.1 allow to directly compare the efficiency of the ionic and electron catalytic routes. At 1000 K, and for the ionic and electron abundances reported in Table C.1, the order in which species dominate is e^- , C^+ , S^+ , Si^+ , H^+ . Note that depending on the abundance of the catalyst and on the temperature, this order can vary. For example, formation by H^+ takes over formation by C^+ for $x(H^+) = 10^{-5}$ and $T_K \geq 10000$ K. However, in dust-free winds, the main physical parameter that changes this order is the photodestruction of the fragile intermediates anion H^- by the visible field. Indeed, as shown by eq. (C.4), the photodetachment of H^- reduces the efficiency of this route for

$$n_H / W < n_H^{crit} = 4.6 \times 10^{14} cm^{-3}. \quad (C.18)$$

This define the boundary ② in Fig. 3. Though, at this critical n_H / W , formation through H^- still dominates over CH^+ route. Assuming that CH^+ is not photodestroyed ($n_H / G_0 > 1.7 cm^{-3}$), formation by C^+ takes over formation by e^- if

$$R_{C^+} \geq R_{elec}. \quad (C.19)$$

Combining eq. (C.17) and (C.8), this condition yields

$$n_H / W \leq 6.7 \times 10^{12} \left(\frac{x(C^+)}{3.6 \cdot 10^{-4}} \right) \left(\frac{x_e}{4.8 \cdot 10^{-4}} \right)^{-1} \left(\frac{T_K}{1000K} \right)^{-1.32} cm^{-3}. \quad (C.20)$$

This equation gives the boundary ③ of Fig. 3.

H_2 can also be formed by three-body reactions with a rate

$$R_{3B} = k^{3B} n_H^3. \quad (C.21)$$

Assuming that electron catalysis is optimal and using eq. (C.21) and (C.8), we find that three-body reaction takes over formation through H^- if

$$n_H \geq 1.9 \times 10^{13} \left(\frac{x_e}{4.8 \cdot 10^{-4}} \right) \left(\frac{T_K}{1000 K} \right)^{1.24} cm^{-3}. \quad (C.22)$$

This defines the boundary ①.

⁷ Assuming an H_2 photodissociation rate of $k = 6 \times 10^{-11} G_0 s^{-1}$.

Dusty. The inclusion of dust does not change the efficiency of gas-phase formation routes but add a new formation route with a rate of

$$R_{dust} = 3.6 \times 10^{-17} \frac{Q}{Q_{ref}} \frac{S(T_K)}{S(1000 \text{ K})} \sqrt{\frac{T_K}{1000 \text{ K}}} n_H^2 \text{ cm}^{-3} \text{ s}^{-1}, \quad (\text{C.23})$$

where the formation rate of Hollenbach & McKee (1979) assuming a single grain size distribution of radius $a_g = \sqrt{\langle r_c^2 \rangle} = 20 \text{ nm}$ and a grain temperature of 15 K is adopted. $S(T_K)$ is the sticking coefficient of H on grain:

$$S(T_K) = \frac{1}{1 + 0.4 \left(\frac{T_K}{100 \text{ K}} + \frac{T_{gr}}{100 \text{ K}} \right)^{0.5} + 0.2 \frac{T_K}{100 \text{ K}} + 0.08 \left(\frac{T_K}{100 \text{ K}} \right)^2}, \quad (\text{C.24})$$

where T_{gr} is the grain temperature. The sticking coefficient does not depend on T_{gr} as long as $T_{gr} \lesssim T_K$ and we adopt $T_{gr} = 15 \text{ K}$ for simplicity.

When gas-phase formation is dominated by H^- , the critical dust fraction ratio above which formation on dust dominate is obtained by combining eq. (C.23) and (C.8):

$$Q/Q_{ref} \geq 9.3 \times 10^{-3} \left(\frac{x_e}{4.8 \cdot 10^{-4}} \right) \left(\frac{T_K}{1000 \text{ K}} \right)^{0.4} \left(\frac{S(T_K)}{S(1000 \text{ K})} \right)^{-1} \frac{\eta}{1 + \eta} \quad (\text{C.25})$$

where η is defined in eq. (C.5). Boundary ⑥ corresponds to the case $\eta \gg 1$, and boundary ⑤ corresponds to the case $\eta \ll 1$. When gas-phase formation route is dominated by CH^+ , formation on dust takes over gas-phase formation for

$$Q/Q_{ref} \geq 1.4 \times 10^{-4} \left(\frac{x(\text{C}^+)}{3.6 \cdot 10^{-4}} \right) \left(\frac{T_K}{1000 \text{ K}} \right)^{-0.92} \left(\frac{S(T_K)}{S(1000 \text{ K})} \right)^{-1}. \quad (\text{C.26})$$

This relation defines the boundary ④.